REVIEW

Check for updates

Recent progress of metal-halide perovskite-based tandem solar cells

Cenqi Yan,[a] Jiaming Huang,[a] Dongdong Li [iD][b] and Gang Li [iD]*[a]

Tandem solar cells (TSCs) are devices made of multiple junctions with complementary absorption ranges, aiming to overcome the Shockley–Queisser limit of single-junction solar cells. Currently, metal-halide hybrid perovskite solar cells have risen as an ideal candidate for various tandem cells due to their high open-circuit voltage, tunable optical bandgap, low energy loss, and low-temperature solution processibility. Herein, the critical advances of perovskite-based tandem cells are presented, including perovskite–silicon, perovskite–perovskite, perovskite–copper indium gallium selenide, and perovskite–organic TSCs. Electrode engineering, interface engineering, bandgap engineering, and processing techniques are discussed in detail. The future directions and challenges of perovskite TSCs are also presented.

Introduction

Due to the intensification of energy resource depletion, the greenhouse effect, and environmental contamination, it has become an urgent task to develop clean and low-carbon-emission energy. Photovoltaics, which directly convert light energy into electricity, is a practical manner of addressing these issues. To date, solar cells based on silicon (Si), gallium arsenide (GaAs), copper indium gallium selenide (CIGS), and cadmium telluride have been commercialized due to their

[a] Department of Electronic and Information Engineering, Research Institute for Smart Energy (RISE), The Hong Kong Polytechnic University, Hung Hom, Kowloon, Hong Kong 999077, P. R. China. E-mail: gang.w.li@polyu.edu.hk
[b] The Interdisciplinary Research Center, Shanghai Advanced Research Institute, Chinese Academy of Sciences, Shanghai, 201210, P. R. China

excellent device performance and mature fabricating techniques. Nonetheless, their fabrication cost-power ratio, rigid form-factor, and deployment cost still restrict the competitiveness of solar cells with conventional fossil energy. The emerging metal-halide perovskite solar cells (PSCs) offer advantages of solution processability, compatibility with large-area deposition techniques,[1] inexpensive and abundant raw materials, and desirable optoelectronic properties such as large extinction coefficient, long ambipolar diffusion lengths, excellent defect tolerance, and low exciton binding energy, rendering PSCs a promising candidate for the next-generation photovoltaic technology. The metal-halide perovskite has the ABX_3 perovskite structure. A stands for monovalent cations, such as methylammonium (MA), formamidinium (FA), cesium (Cs), or their combination; B refers to divalent metal elements, such as lead (Pb), tin (Sn), copper (Cu), manganese (Mn), and germanium (Ge); and X denotes

Cenqi Yan is currently a Postdoctoral Research Scholar in the Department of Electronic and Information Engineering, Hong Kong Polytechnic University. She received her BS degree in Material Physics from Shandong University in 2013 and her PhD degree in Mechanics (Advanced Materials and Mechanics) from Peking University in 2018. Her current research focuses on organic solar cells and perovskite solar cells.

Cenqi Yan

Jiaming Huang received his bachelor's degree from Guangxi University in 2016 and master's degree from Ningbo institute of Materials Technology and Engineering, Chinese Academy of Science in 2019. Currently, he is a PhD candidate in the Department of Electronic and Information Engineering, Hong Kong Polytechnic University. His research interest focuses on flexible electronics.

Jiaming Huang

halogen elements, including chlorine (Cl), bromine (Br) and iodine (I). By far, the power conversion efficiency (PCE) of PSCs has achieved 25.5%,[2–5] thereby attracting substantial attention from both academia and industry.

Since the invention of the solar cell in 1954, intensive efforts have been invested in improving the PCE of photovoltaic cells. Early in 1961, Shockley and Queisser published the principle of detailed balance which unveiled the thermodynamic upper limit of p–n junction solar cells.[6] They premised four commonly accepted assumptions. (1) One incident photon generates one electron–hole pair; (2) photons with larger energy than the E_g of photoactive materials are absorbed, while those with lower energy than the bandgap (E_g) do not contribute to photogeneration of charge carriers; (3) the photovoltaic device is free of non-radiative recombination; (4) the incident light is neither concentrated nor anisotropic. As the Shockley–Queisser (S–Q) limit points out, a single-junction solar cell cannot exceed 33.16% efficiency under standard AM 1.5G illumination. The thermalization loss and transmission loss principally limit the efficiency of single-junction solar cells. Thermalization loss is mainly caused by the thermal relaxation of the excited electron to the band edge when the absorbed photon energy is more than E_g; transmission loss resulted from the fact that the photons with energy smaller than E_g are not absorbed.

Tandem architecture is recognized as a promising method to overcome the S–Q limit of the single-junction cells. In a tandem device, the incident light impinging on the tandem device penetrates top subcells and bottom subcells sequentially. Typically, the upper subcell employs a wide-E_g absorber that harvests photons with higher energy, while lower-energy photons are absorbed by the bottom subcell using narrow-E_g materials. Consequently, the theoretical PCE limit for a two-subcell tandem device is up to ∼42% and can be further improved to ∼68% for the infinite-subcell device.

Metal-halide perovskites are an ideal component of tandem solar cells (TSCs) for the following reasons. Firstly, metal halide perovskites are sound light absorbers for the top and bottom subcells because their optical bandgaps can be adjusted in the range of 1.17–3.10 eV through composition engineering. Secondly, the high structural tolerance of perovskite reduces the stringent requirements for lattice matching between subcells. The electrical tolerance of perovskite effectively reduces the deep defect centers coming from surface and bulk defects caused by lattice mismatch between subcells. PSCs are compatible with solution and vacuum fabrication methods, and n–i–p and p–i–n device structures. The abovementioned merits of PSCs facilitate the construction of all-perovskite TSCs, and the collaboration of perovskites and established crystalline Si (c-Si), CIGS solar cells, or organic solar cells to construct hybrid TSCs with respectable PCEs.

Herein, we first introduce the basic configuration of perovskite solar cells, four-terminal (4-T) and two-terminal (2-T) tandem structures. Then we present the recent advancement of perovskite TSCs, including perovskite–c-Si, perovskite–perovskite, perovskite–CIGS, and perovskite–organic tandems, where the aspects of electrode engineering, interface engineering, bandgap engineering, composition engineering, and processing techniques, are discussed in detail. The architecture and performance of the perovskite-based TSCs are summarized in Table 1. Lastly, we discuss the future directions and challenges of the commercialization of perovskite TSCs.

1. Configuration of TSCs

Generally, TSCs can be mainly designed as a mechanically stacked 4-T cell, a 4-T cell with optical splitter, or a monolithic 2-T device (Fig. 1). In a 4-T configuration, top and bottom subcells are connected through an electrical circuit, enabling the independent fabrication of top and bottom subcells. Circuit management is simplified, and the total efficiency is simply the sum PCE of two subcells. 4-T cell can be constructed using an

Dongdong Li received his PhD degree in Materials Science from Shanghai Jiaotong University in 2010. Under the support of the Ministry of Education of the People's Republic of China, he worked in the Department of Electrical Engineering at the University of Southern California (2007–2009). Currently, he is a professor at Shanghai Advanced Research Institute, Chinese Academy of Sciences. His research focuses on functional thin films with various nanostructures and tunable optoelectronic properties, for applications in high efficiency solar cells, and neuromorphic computing devices, etc.

Dongdong Li

Dr Gang Li is a Sir Sze-yuen Chung Professor in Renewable Energy in the Hong Kong Polytechnic University. His research interests are the materials, device engineering and device physics in organic semiconductors and hybrid perovskite semiconductors. He obtained his BS degree from Wuhan University, MS and PhD from Iowa State University, respectively. He was a research professor in UCLA, and VP of Solarmer Energy Inc. He is a Thomson Reuters/Clarivate Analytics Highly Cited Researcher (2014–2020), published ∼150 papers with ∼64 000 citations and h-index of 74. He is a Fellow of the Royal Society of Chemistry (FRSC), and SPIE (FSPIE).

Gang Li

Materials Chemistry Frontiers

Table 1 Summary of the structure and performance of perovskite-based tandem solar cells

Absorber	E_g [eV]	Transparent electrode	ICL	V_{OC} [mV]	J_{SC} [mA cm^{-2}]	FF [%]	PCE [%]	Total PCE [%]	Ref.
$MAPbI_3$	~1.6	MoO_x/ITO	—	821	14.5	51.9	6.2	13.4	9
SHJ	~1.1			689	13.7	76.7	7.2		
$MAPbI_3$	~1.6	$AZO/ITO/MgF_2$	—	952	16.5	77.4	12.3	18.0	10
Mono-Si	~1.1			562	13.3	76.2	5.7		
$MAPbI_3$	~1.6	MoO_x/IZO	—	870	17.5	68	10.36	18.18	11
SHJ	~1.1			690	14.6	77.6	7.82		
$MAPbI_3$	~1.6	IZO	—	938	17.36	59.6	9.71	18.19	
SHJ	~1.1			693	15.81	77.44	8.48		
$Cs_{0.05}FA_{0.81}MA_{0.14}PbI_{2.55}Br_{0.45}$	1.63	$MoO_3/IZO/MgF_2$	—	1120	22.3	77.7	19.4	28.6	12
SHJ	~1.1			700	17.2	76.6	9.2		
$MAPbI_3$	~1.6	Cu/Au	—	1080	20.6	74.1	16.5	23.0	101
SHJ	~1.1			679	12.3	77.9	6.5		
$MAPbI_3$		AgNW	—	1025	17.5	71	12.7	17.0	17
mc-Si				547	11.1	70.4	4.3		
$MAPbI_3$		MoO_x/AuNW/MoO_x	—	1156	19.8	79.9	18.3	27.0	18
SHJ				698	15.6	80.1	8.7		
$MAPbI_3$		Graphene	—	900	12.6	55	6.2	13.2	19
SHJ				670	14	73.8	7		
$MAPbI_3$		Optical splitter	—	987	10.6	71.5	7.5	28	22
SHJ				728	34.9	80.9	20.5		
$MAPbI_3$	~1.6		n++/p++ Si tunnelling junction	1580	11.5	75		13.7	23
c-Si	~1.1								
$MAPbI_3$			ALD SnO_2	1780	14	79.5		19.9	24
SHJ									
$MAPbI_3$			IZO	1692	15.8	79.9		21.4	25
SHJ									
$MAPbI_3$			SnO_2	1676	16.1	78		21	26
Homo-junction Si									
$MAPbI_3$			SnO_2	1660	15.6	68		17.6	
Homo-junction Si									
$(FAPbI_3)_{0.83}(MAPbBr_3)_{0.17}$			SnO_2	1740	16.2	78		21.9	27
Homo-junction Si									
$(FAPbI_3)_{0.83}(MAPbBr_3)_{0.17}$			SnO_2	1730	16.5	81		23.1	28
Homo-junction Si									
$Cs_{0.05}Rb_{0.05}FA_{0.765}MA_{0.135}PbI_{2.55}Br_{0.45}$	1.63		TiO_2	1763	17.8	78.1		24.5	29
SHJ									
$Cs_{0.05}(MA_{0.17}FA_{0.83})Pb_{1.1}(I_{0.83}Br_{0.17})_3$			ITO	1760	18.5	78.5		25.5	30
SHJ									
$Cs_{0.05}(FA_{0.83}MA_{0.17})_{0.95}Pb(I_{0.8}Br_{0.2})_3$			nc-SiO_2:H/ITO	1791.9	19.02	74.6		25.43	102
SHJ									
$Cs_{0.05}MA_{0.15}FA_{0.8}PbI_{2.25}Br_{0.75}$			NiO_x/InO_x	1780.5	19.07	75.36		25.7	32
SHJ									
$Cs_{0.1}MA_{0.9}Pb(I_{0.9}Br_{0.1})_3$			ITO	1820	19.2	75.3		26.2	33
SHJ									
$FA_{0.5}MA_{0.38}Cs_{0.12}PbI_{2.04}Br_{0.96}$	1.69		ITO	1655	16.5	81.1		22.22	42
SHJ									
$(FA_{0.65}MA_{0.2}Cs_{0.15})Pb(I_{0.8}Br_{0.2})_3$	1.68		ITO	1756	19.2	79.2		26.7	45
SHJ	1.12								
$FA_{0.75}Cs_{0.25}Pb(I_{0.85}Br_{0.15})$:2 to 5 mol% $MAPbCl_3$	1.67		—	1886	19.12	75.3		27.13	43
SHJ									
$MAPb(I_{0.95}Br_{0.05})_3$	~1.6		ITO	1670	18.29	77		23.5	47
SHJ	1.1								
CsFAPbIBr	~1.77		IZO	2700				13.2	49
CsFAPbIBr	~1.55		nc-Si:H						
SHJ									
$MAPbBr_3$	2.2		PCBM:P3HT	1950	8.4	66		10.8	51
$MAPbI_3$	1.58								
$MAPbI_3$	1.58	ITO	—	1080	16.69	75	13.52	19.08	55
$MA_{0.5}FA_{0.5}Pb_{0.75}Sn_{0.25}I_3$	1.33			760	9.14	80	5.56		
$FA_{0.83}Cs_{0.17}Pb(I_{0.5}Br_{0.5})_3$	1.8		SnO_2/ZTO/ITO	1660	14.5	70		16.9	56
$FA_{0.75}Cs_{0.25}Sn_{0.5}Pb_{0.5}I_3$	1.2								
$FA_{0.83}Cs_{0.17}Pb(I_{0.83}Br_{0.17})_3$	1.6	ITO	—	970	20.3	79	15.7	20.1	
$FA_{0.75}Cs_{0.25}Sn_{0.5}Pb_{0.5}I_3$	1.2			740	7.9	73	4.4		
$FA_{0.3}MA_{0.7}PbI_3$	~1.58	MoO_x/Au/MoO_x	—	1141	20.1	80.0	18.3	21.2	59
$(FASnI_3)_{0.6}(MAPbI_3)_{0.4}$	1.25			808	4.8	74.4	2.9		
$FA_{0.8}Cs_{0.2}Pb(I_{0.7}Br_{0.3})_3$	1.75		Ag/MoO_x/ITO	1922	14	78.1		21	60
$(FASnI_3)_{0.6}(MAPbI_3)_{0.4}$:Cl	1.25								
$FA_{0.6}Cs_{0.4}Pb(I_{0.65}Br_{0.35})_3$	1.8		SnO_2/ITO/PEDOT:PSS	1990	15.1	77		23	62
$FA_{0.5}MA_{0.45}Cs_{0.05}Pb_{0.5}Sn_{0.5}I_3$:Cd	1.22								

Table 1 (*continued*)

| Absorber	E_g [eV]	Transparent electrode	ICL	V_{OC} [mV]	J_{SC} [mA cm^{-2}]	FF [%]	PCE [%]	Total PCE [%]	Ref.
$Cs_{0.2}FA_{0.8}PbI_{1.8}Br_{1.2}$	1.77		SnO_2/Au/PEDOT:PSS	1965	15.6	81		24.8	63
$MA_{0.3}FA_{0.7}Pb_{0.5}Sn_{0.5}I_3$	1.22								
$CS_{0.05}FA_{0.8}MA_{0.15}PbI_{2.55}Br_{0.45}$	1.63	IZO	—	1124	20.8	79.3	18.5	25.4	65
$(FASnI_3)_{0.6}(MAPbI_3)_{0.4}$	~1.25			806	10.5	80.6	6.8		
$Cs_{0.05}FA_{0.8}MA_{0.15}PbI_{2.55}Br_{0.45}$	1.75		—	1942	15.01	80.31		23.4	
$(FASnI_3)_{0.6}(MAPbI_3)_{0.4}$	~1.25								
$MAPbI_3$			ITO	1353	5.6	60.4		4.6	76
$Cu_2ZnSn(S, Se)_4$	1.1								
$MAPbI_3$		AgNW	—	1025	17.5	71	12.7	18.6	17
CIGS				682	10.9	78.8	5.9		
$MAPbI_3$		In_2O_3:H	—	1104	17.4	73.6	14.1	20.4	68
CIGS				667.4	12.7	74.9	6.3		
Perovskite				1450	12.7	56.6		10.9	69
CIGS									
$(FA_{0.65}MA_{0.20}Cs_{0.15})Pb(I_{0.8}Br_{0.2})_3$	1.68	IZO		1137	19.6	76.8	17.1	25.9	71
CIGS	1.12			715	15.6	79.2	8.8		
$Cs_5(MA_{17}FA_{83})_{95}Pb(I_{83}Br_{17})_3$	1		AZO/SAM	168	19.17	71.9		23.16	74
CIGS									
$Cs_{0.09}FA_{0.77}MA_{0.14}Pb(I_{0.86}Br_{0.14})_3$	1.59		ITO/PTAA	1773.9	17.3	73.1		22.43	75
CIGS	1								
$MAPbI_3$	1.52		PFN/TiO_2/PEDOT:PSS	1520	10.05	67		10.23	84
PBSeDTEG8:PCBM									
$CsPbBr_3$	2.3	PH 1000	—	1380	6.15	70.51	5.98	14.03	83
PBDB-T-SF:IT-4F				880	12.18	75.16	8.05		
$FAPbBr_{2.43}Cl_{0.57}$	2.36		ZnO-NP/ITO	2230	6.61	74		10.83	85
PTB7-Th:6TIC-4F									
$Cs_{0.1}(FA_{0.6}MA_{0.4})_{0.9}Pb(I_{0.6}Br_{0.4})_3$	1.74		PEDOT/Ag/BCP	1850	11.52	70.98		15.13	86
PBDB-T:SN6IC-4F	1.30								
$Cs_{0.1}(FA_{0.6}MA_{0.4})_{0.9}Pb(I_{0.6}Br_{0.4})_3$	1.74		PEDOT/Ag/BCP	1800	11.07	68.31		13.61	
PBDB-T:SN6IC-4F	1.30								
$FA_{0.8}MA_{0.02}Cs_{0.18}PbI_{1.8}Br_{1.2}$	1.77		$BCP/Ag/MoO_3$	1902	13.05	83.1		20.6	88
$PM6:PC_{71}BM:Y6$	1.41								
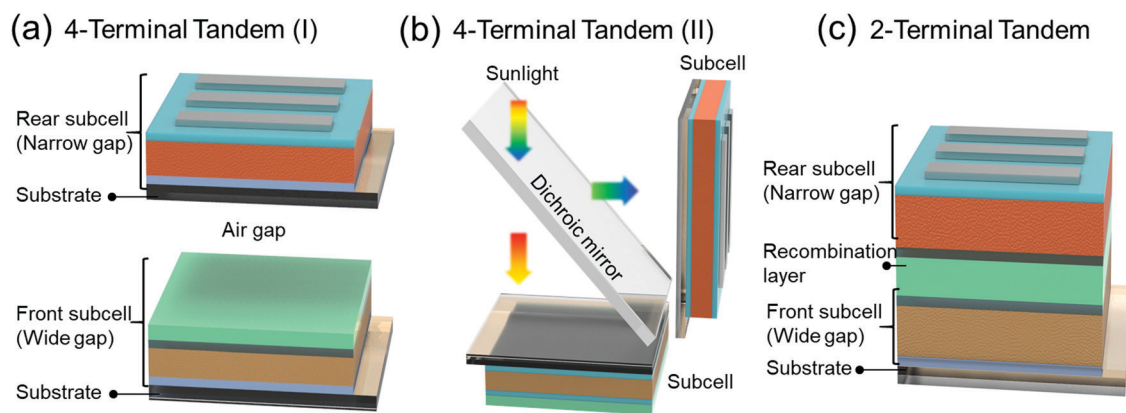
Fig. 1 Structures of (a) a mechanically stacked four-terminal cell, (b) a four-terminal cell with an optical splitter, and (c) a monolithic two-terminal cell.

optical splitter with high reflection in the short-wavelength range and high transmission in the long-wavelength range. *Via* optical splitter, subcells in a 4-T structure can be set spatially separated yet optically coupled. In a 2-T monolithic tandem architecture, the two subcells are directly joined through an interconnecting layer (ICL) instead of an electrical circuit to form a tandem device. The ICL layer between two subcells, such as the tunnelling junction and recombination layer, strongly influences the charge carrier transport and current loss. Compared with the 4-T structure, the monolithic 2-T architecture has fewer fabrication steps, transparent conducting electrodes, and encapsulation materials, resulting in much lower manufacturing cost and less parasitic absorption. However, monolithic tandems require strict processing compatibility: (i) both subcells should be optimized to produce similar current densities at maximum power point (MPP), as the tandem current density is limited by the lower current density of two subcells. (ii) The later formed cell should be processed at low temperatures and *via* orthogonal solvent in the presence of the temperature and solvent-sensitive former formed cell.

2. Perovskite–silicon TSCs

c-Si solar cells have occupied over 90% share of the global photovoltaic market with highly mature manufacturing lines and supply chains. Currently, the single-junction c-Si cell has reached a high PCE of 26.7%,[7,8] closely approaching the theoretical limit of 29.4%. Furthermore, c-Si presents a low E_g of 1.12 eV, which renders Si solar cells highly suitable as the narrow bandgap bottom cell in TSCs. The perovskite–c-Si tandems, where perovskites can effectively improve efficiency with little additional cost, are presumably the most direct pathway to commercializing PSCs. It is a shortcut to improving commercial c-Si efficiencies, associated with significant financial benefit considering that the global solar photovoltaic Panels market size has been steadily growing and surpassed $130 billion in 2020, and every 1% higher module efficiency means profit of $\sim$\$5 billion.

2.1 Perovskite–silicon 4-terminal TSCs

Semi-transparent perovskite solar cells (ST-PSCs) are the pre-requisite and challenge of perovskite–Si 4-T TSCs. The transparent electrode of ST-PSCs should have both high transparency to ensure the photon harvesting of the bottom cell and high lateral conductivity to minimize current loss. Besides, transparent electrodes should have processing compatibility with the layers beneath. More specifically, the fabrication of top transparent electrodes should use low-temperature deposition and mild precursors to prevent or minimize the damage to the underlayer interlayer and perovskite layer. Besides, they should have appropriate energy levels. Transparent electrodes of optoelectronic devices can be made of thin metal films, conductive oxides, metal nanowires, dielectric/metal/dielectric (DMD) photonic structures, conductive polymers, carbon nanotubes, graphene, and so forth.

In 2014, the Ballif group pioneered constructing the perovskite–c-Si TSC with a MoO_x/indium tin oxide (ITO) transparent electrode.[9] The 30 nm MoO_x layer functioned as a hole-collecting buffer layer to prevent the harm of ion bombardment during ITO sputtering, and the 100 nm ITO layer provided lateral conductivity

and broad-band transparency. The $MAPbI_3$ top cell demonstrated a transmittance $> 55\%$ in the near-infrared (NIR) region, allowing the bottom cell with a short-circuit current density (J_{SC}) of 13.7 mA cm^{-2}. The 4-T tandem device yielded a sum efficiency of 13.4% from the 6.2%-efficiency $MAPbI_3$ top cell and 7.2%-efficiency filtered silicon heterojunction (SHJ) bottom cell, exceeding the $MAPbI_3$ solar cell with a MoO_x/Ag electrode (11.6%). McGehee and coworkers utilized aluminium-doped (2 mol%) zinc oxide (AZO) nanoparticles to solution-deposit an electron-selective buffer layer atop PCBM. The aluminium dopant eliminates the extraction barrier arising from the misaligned work functions of ZnO and ITO. A sum PCE of 18.0% is realized for 4-T tandem, based on the 12.3%-efficiency ST-PSC and 5.7%-efficiency filtered Si solar cells, exceeding the 17.0%-efficiency mono-Si reference.[10] The Ballif group sputtered an amorphous indium zinc oxide (IZO) layer to fabricate a transparent electrode, which absorbed $< 3\%$ in the 400–1200 nm wavelength range and exhibited a sheet resistance of 35 Ωsq^{-1}. Over 9% efficiency was achieved in ST-PSCs with IZO directly sputtered on spiro-OMeTAD, and the efficiency was increased to 10.3% with the insertion of MoO_x. The corresponding 4-T tandem devices with and without MoO_x buffer layer both achieved similar PCEs of 18.18% and 18.19%, revealing the trade-off between reduced sputter damage and increased parasitic absorption of MoO_x.[11] The reported PCE values of the tandems have so far lain below their potential owning to inefficient photon harvesting. Sargent and coworkers used the MoO_3/IZO/MgF_2 transparent electrode to realize a 19.4% PCE for 1.63 eV ST-PSCs with an average near-infrared transmittance of 85%. With a boosted solvent extraction technique (BSE), they increased the optical path length of the triple-cation perovskite ($Cs_{0.05}FA_{0.81}MA_{0.14}PbI_{2.55}Br_{0.45}$) films by preserving homogeneous and smooth morphology at a thick perovskite layer.[12] In the BSE approach, the spin-coating speed is raised precisely one second before anti-solvent dripping, facilitating the lateral hydrodynamic flow and evaporation of the mixed solvents, and thus the rapid nucleation of the intermediate phase. As Fig. 2a shows, X-ray diffraction patterns of intermediate phases in the unannealed perovskite films prepared by the BSE method exhibited narrower
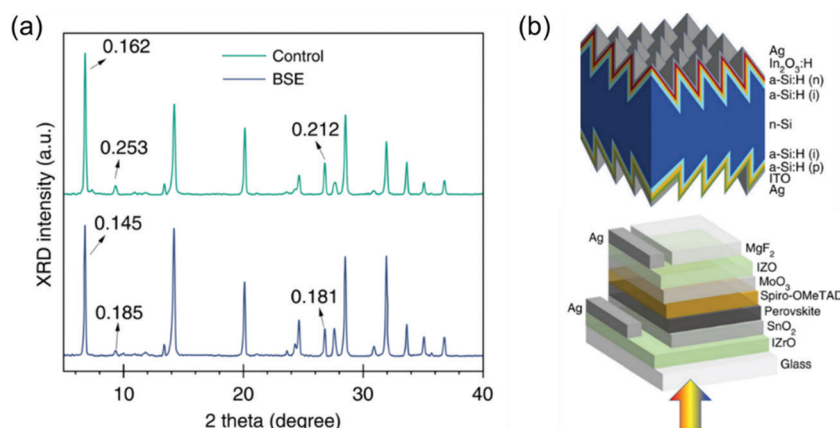

Fig. 2 (a) X-Ray diffraction pattern of unannealed perovskite films fabricated by non–BSE and BSE methods. The numbers refer to the full width at half maximum. (b) Device architectures of mechanically stacked TSCs, consisting of a perovskite top cell and SHJ bottom cell.[12]

peak width, illustrating the excess solvent in the unannealed control film, as the local structural order therein can be interrupted by DMSO/DMF over incorporation (Fig. 2a). The enhanced surface morphology can improve the photovoltaic performance, and the urea is further added as a Lewis base to decrease the trap density and increase the electron diffusion length to 2.3 μm. The couple of ST-PSCs and a 9.2%-efficiency filtered silicon bottom cell yields a 28.6% 4-T tandem (Fig. 2b).

An ultra-thin metal film is an alternative approach for transparent electrodes by its good transmittance and conductivity. In 2014, Snaith and coworkers reported that the thermal-evaporation of 10 nm Au on spiro-OMeTAD and the creation of a microporous perovskite layer by partial dewetting of solution-cast films enabled ST-PSCs with $\sim$8% efficiency and $\sim$30% transmittance in the visible region.[13] However, Au fails to form a uniform, continuous, and ultra-thin film due to the Volmer–Weber growth mechanism, which reduces the transmittance and increases the corresponding electrodes' sheet resistance. To improve Au's film-forming properties at a small thickness, Cheng and coworkers designed a sandwiched MoO_x–Au–MoO_x stack as a transparent electrode.[14] MoO_x has good hole injection capability and provides a good nucleation surface to form a thin yet uniform Au film. The top MoO_x layer works as an anti-reflection layer. In their work, the semi-transparent $MAPbI_3$ device shows a PCE of 5.3% with 31% average visible transmittance (AVT), and a PCE of 13.6% with 7% AVT. Parallelly, Yang and coworkers designed a MoO_x (10 nm)–Au (1 nm)–Ag (10 nm)–MoO_x (40 nm) multi-layer transparent top electrode for PSCs.[15] The gold seeded silver film exhibited superior conductivity and optical transparency to pristine Ag or Au, owning to Au's higher surface energy. The ST-PSC illuminated from the DMD top electrode afforded 11.5% efficiency and exhibited almost no open-circuit voltage (V_{OC}) and fill factor (FF) loss compared with the opaque device. Likewise, the Huang group designed a Cu (1 nm)/Au (7 nm) metal electrode for semi-transparent $MAPbI_3$ PSCs.[16] At a thin film, Au atoms are more strongly coupled to each other, leading to the formation of Au islands via Volmer–Weber growth during thermal evaporation. As Cu exhibits a larger surface energy of 1790 mJ m^{-2} than Au (1506 mJ m^{-2}), Au atoms preferentially attach to Cu, resulting in continuous ultrathin Au films via Frank–van der Merve growth (Fig. 3a). ST-PSCs under front illumination exhibit a PCE of 16.5%, a high FF of 74.1%, and a J_{SC} of 20.6 mA cm^{-2}, illustrating that the Cu/Au transparent electrodes induce little loss during the collection and lateral transport of photogenerated charges (Fig. 3b). Under rear illumination, the device exhibits a PCE of 12.1% with a smaller J_{SC} of 15.2 mA cm^{-2}, ascribed to the less transparency of the Cu/Au/BCP layer than ITO in the visible spectrum. As Fig. 3c shows, opaque PSCs and semi-transparent devices under front illumination have comparable EQE values at short wavelengths (300–550 nm), while semi-transparent devices exhibit lower EQE at longer wavelengths (600–800 nm). When illuminated through the semi-transparent PSC, a SHJ solar cell operates with a 6.5% efficiency, leading to a sum PCE of 23.0% for the 4-T tandem device.

Metal nanowire offers the advantage of easy deposition in a room-temperature solvent-free process, in addition to low sheet resistance and high optical transmission. McGehee and coworkers afforded a 12.7%-efficiency semi-transparent $MAPbI_3$ PSC with a AgNW electrode, which was first sprayed on flexible polyethylene terephthalate (PET), and then mechanically transferred to the spiro-OMeTAD layer. A sum PCE of 17.0% was realized when the semi-transparent PSC was mechanically placed on multi-crystalline Si cells (unfiltered: 11.4%, filtered: 4.3%).[17] Yang, Liu, and coworkers designed a sandwiched MoO_3/gold nanowire (AuNW) mesh/MoO_3 transparent electrode.[18] The large surface tension of MoO_3 effectively improved Au's wettability, resulting in Frank–van der Merwe growth to produce an ultrathin AuNW mesh layer. The top MoO_3 layer reduces the reflections at the gold layer to increase light transmission. A sum efficiency of 27.0% is realized when they mechanically stacked the 18.3% efficiency semi-transparent $MAPbI_3$ PSC on a SHJ rear cell (unfiltered: 23.3%, filtered: 8.7%).

Graphene-based electrodes have a high optical transmission of 97.4% with a sheet resistance of 100 Ωsq^{-1}.[19] The Yan group pioneered laminating chemical vapor deposition (CVD) stacked graphene as a transparent electrode.[20] They further coated a PEDOT: PSS layer atop graphene, which significantly improved the electrode's conductivity and provided adhesivity for lamination (Fig. 4a and b). The sheet resistance was decreased to about 260 Ωsq^{-1} by the doping effect of PEDOT:PSS (Fig. 4c). As Fig. 4d shows, the two-layer graphene doped with PEDOT: PSS has an R_s of 140 Ωsq^{-1} and a transmittance >90% in the
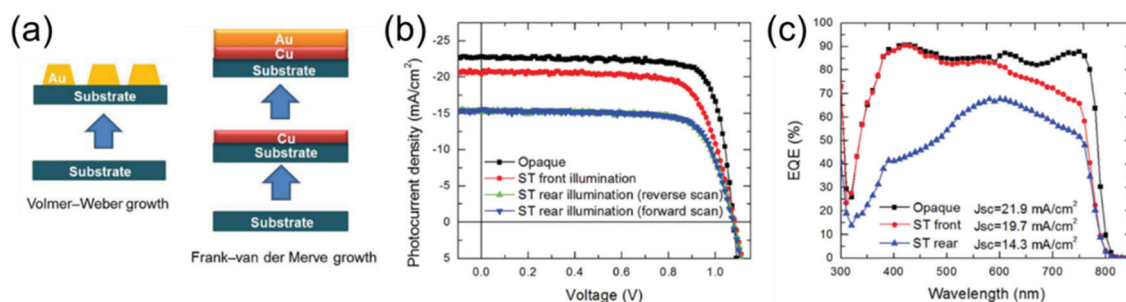

Fig. 3 (a) Scheme of Volmer–Weber growth and Frank–van der Merve growth. (b) J–V curves of opaque and semitransparent PSCs. (c) EQE curves of opaque and ST-PSCs under front and rear illumination.[16]
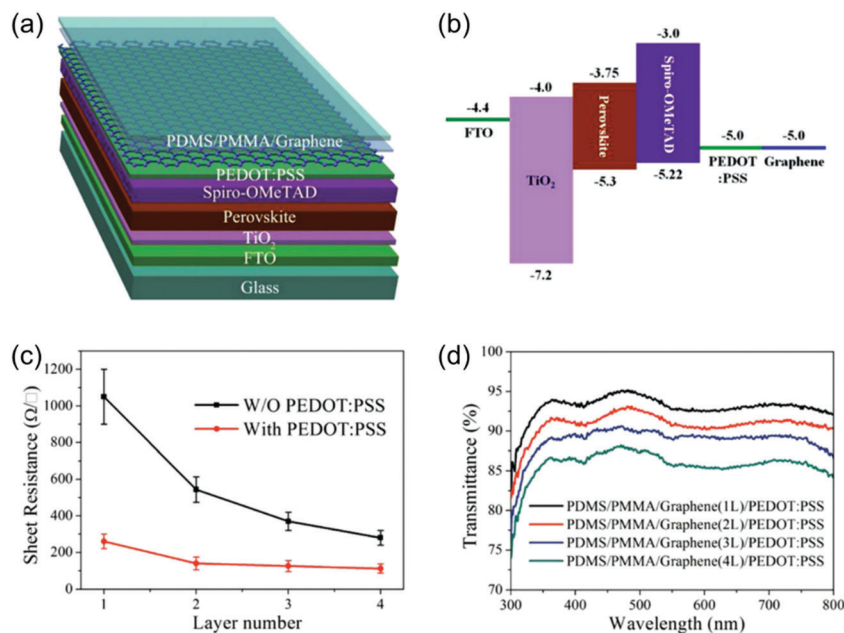
Fig. 4 (a) Device architecture of a semi-transparent PSC. (b) Energy level distribution of layers of semi-transparent PSCs. (c) The sheet resistance of 1–4 layers of stacked graphene films with and without PEDOT:PSS. (d) UV-vis transmittance spectra of PEDOT:PSS doped transparent graphene electrodes.[20]

visible region. When the layers of graphene further increase, the sheet resistance was further decreased, and the transmittance was below 90%. The ST devices with double-layer graphene electrodes show PCEs of 12.37% and 12.03% from the FTO and graphene sides, respectively (Fig. 4d).

Lang and coworkers[19] showed the successful implementation of a transparent large-area, high-quality, single-layer graphene contact upon spiro-OMeTAD in PSCs. The van der Waals forces ensured the adhesion and intimate contact of graphene on spiro-OMeTAD and enabled a 6.2%-efficiency semi-transparent cell in the absence of an additional auxiliary layer. The ST-PSC and the SHJ solar cell (unfiltered: 18.5%, filtered: 7.0%) are assembled into a 4-T tandem device, giving a higher PCE of 13.2% than single-junction PSCs with typical Au contacts (10.2%).

In the perovskite–silicon 4-T TSCs, the top PSCs are commonly stacked onto the bottom c-Si devices with an air gap. Due to the significant refractive indices mismatch between the air and functional layers, a part of the NIR light would be reflected to the PSCs. In 2018, Jaysankar and coworkers proposed a refractive index matching layer (IML) to replace the unfavourable air gap.[21] The introduction of the optical spacer increased the transmission of NIR light through the top PSC and boosted the photocurrent of the c-Si bottom solar cell.

Although mainstream 4T TSCs adopt the "planar structure" aforementioned, in principle they can be constructed using other configurations. For example, an optical splitter is a multi-layer beam splitter with high reflection in the short-wavelength range and high transmission in the long-wavelength range. By splitting the incident solar spectra and distributing them to each subcell, solar energy can be utilized more effectively. Via an optical splitter, subcells in 4-T structure can be set spatially separated yet optically coupled (Fig. 5). The optical splitter is fabricated by sputtering multi-layer dielectric oxides with high ($n \sim 1.9$–2.2) and low ($n \sim 1.5$) refractive indices on both sides of the glass. The cut-off wavelength can be controlled by altering the number and thickness of the stacking layers. The Yamamoto group designed a series of optical splitters with cut-off wavelengths of 550, 600, and 640 nm, respectively.
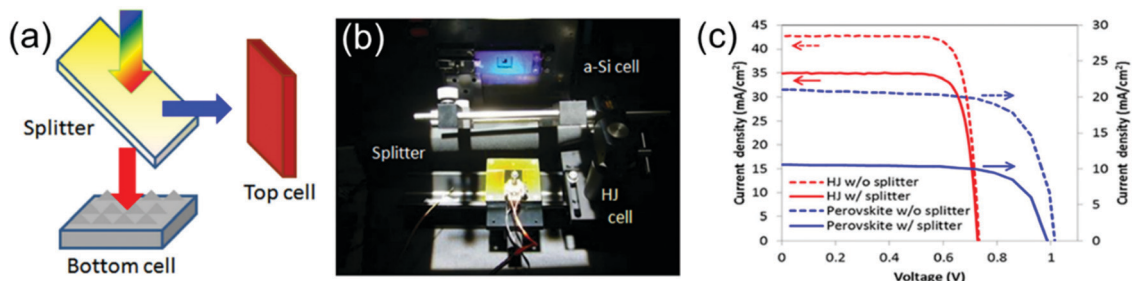

Fig. 5 (a) Scheme of the optical splitting system, (b) measurement setup of an optical splitting system, and (c) J–V curves of SHJ and perovskite solar cells with and without a splitter.[22]

They achieved 28%-efficiency 4-T devices based on 7.5%-efficiency $MAPbI_3$ PSCs and SHJ solar cell (unfiltered: 25.2%, filtered: 20.5%) with an optical splitter featuring 550 nm cut-off wavelength.[22]

2.2 Perovskite–silicon 2-terminal TSCs

The 2-T configuration, where subcells are constructed as a single integrated unit, allows simple electrical integration and bypasses additional transparent electrodes. Nonetheless, the monolithic approach requires a tunnelling/recombination interlayer that can effectively facilitate the flow of photogenerated carriers between two subcells. A reasonable tunnelling/recombination layer should introduce small electrical and optical losses and low processing costs.

Si is an indirect-E_g semiconductor. It is common to design tunnelling junctions consisting of two heavily doped p++ and n++ regions for charge recombination. McGehee and coworkers demonstrated the first 2-T monolithic perovskite–silicon TSC with an inter-band tunnelling junction.[23] To form n++/p++ tunnelling junction, they deposited heavily doped n++ hydrogenated amorphous silicon (a-Si:H) on the p++ emitter *via* plasma-enhanced chemical vapor deposition (PECVD) and subsequently thermally annealed the a-Si:H layer to activate the dopants. Besides, a 2–3 nm-thick intrinsic a-Si layer was inserted between the p++ emitter and n++ amorphous Si layer to mitigate the dopant interdiffusion and prevent the degrading of the tunnelling-junction conductivity. They obtained a PCE of 13.7% and a V_{OC} of 1.58 V for the 1 cm^2, 2-T $MAPbI_3$/Si tandem device. The slow current-dynamics and corresponding hysteresis of the tandem device resembled the sluggish dynamics of the $MAPbI_3$ PSC, which indicated that the perovskite subcell limited the J_{SC} of the TSCs. The n++/p++ tunnelling junction demonstrated high shunt resistances and potentially facilitated the fabrication of large-area tandems. However, this Si-based tunnelling junction requires an additional PECVD step and introduces parasitic optical absorption.

The transparent conductive oxide (TCO) recombination layer is an alternative for constructing 2-T devices, like indium-doped tin oxide (ITO) and indium-doped zinc oxide (IZO). Before 2015, the reported c-Si/perovskite tandems usually required high-temperature (~ 500 °C) processing to sinter mesoporous TiO_2. This processing is not compatible with the best-performing SHJ technology, as a-Si:H requires the temperature to remain below 200 °C. To tackle this problem, Grätzel and coworkers sputtered the ITO recombination layer and used the atomic layer deposition (ALD) SnO_2 layer as the electron selective contact for PSCs to construct a 2-T perovskite-SHJ tandem architecture.[24] The 2-T devices demonstrate an efficiency of 19.9%, with a J_{SC} of 14 mA cm^{-2}, a V_{OC} of 1.78 V, and FF of 79.5%. In their work, the SHJ structure's potential is not completely fulfilled due to the absence of a pyramid texture on the Si wafer, as the solution processing of PSCs requires a smooth substrate underneath. The Ballif group chose an IZO recombination layer in the 2-T monolithic perovskite–Si tandem cell, which is inspired by the successful application of the IZO recombination layer in organic tandem solar cells.[25]

They presented low-temperature-processing $MAPbI_3$/SHJ monolithic TSCs with efficiencies of 19.2% with an aperture area of 1.22 cm^2 and 21.2% with 0.17 cm^2 aperture area, respectively. According to transfer matrix simulations, the PSCs can achieve a maximum current density of the top cell with a ~ 40 nm thick IZO recombination layer and a 150 nm thick spiro-OMeTAD layer, and the SHJ bottom cell needs to be textured to harvest more infrared photons. Impediments to more advances in TCO interlayer include substantial parasitic absorption due to free-carrier absorption at long wavelengths and the proneness of carriers to be funnelled to shunt paths along the recombination layer, which limits large-area fabrication.

In general, an interface (tunnelling or recombination) layer makes electrical contact between the top and the bottom subcells but incurs higher fabrication costs and parasitic absorption. The "interlayer-free" concept offers the advantages of more straightforward processing and reduced optical losses. For the first time, Baillie group demonstrated a monolithic planar-$MAPbI_3$ perovskite-homo-junction silicon tandem without the use of an additional interface layer.[26] The mechanism is that the solution-processed SnO_2 layer serves as an electron transport layer for the perovskite top cell and as a recombination layer between the perovskite top cell and the Si bottom cell. The champion 2-T device with a 4 cm^2 area achieves a steady-state efficiency of 20.5% when the PDMS foil is applied. Besides, upscaling to large-area devices becomes straightforward as the monolithic tandem device relies on the p++ emitter instead of SnO_2 for lateral conduction. Thereby, a steady-state PCE of 17.1% can be achieved in a large area of 16 cm^2. They further optimize the device structure in some aspects. First, a new metal grid design is used for demonstrating 16 cm^2 large-area devices. Second, the planar homojunction silicon subcell is replaced with a textured homojunction silicon bottom cell. Third, a mixed perovskite absorber $(FAPbI_3)_{0.83}(MAPbBr_3)_{0.17}$ is used instead of $MAPbI_3$, which can improve the V_{OC} of the tandem device and reduce hysteresis, owing to the larger E_g and better quality of mixed perovskite. Correspondingly, they demonstrated a 16 cm^2-area perovskite–homojunction silicon tandem device with a high PCE of 21.9% under reverse scan and a high FF of 78%.[27]

Parasitic UV absorption and UV-induced degradation by spiro-OMeTAD in PSCs hinder device performance and stability when the perovskite cell is a top cell of perovskite–Si TSCs. Hence, the Baillie group applied textured polydimethylsiloxane (PDMS) films that incorporate a down-shifting material, (Ba, Sr)$_2$SiO$_4$:Eu^{2+} micron phosphor, in front of the monolithic 2-T perovskite–homojunction silicon tandem device (Fig. 6a).[28] (Ba,Sr)$_2$SiO$_4$:Eu^{2+} phosphor had high luminescent efficiency with broad UV absorption and short decay time, which is suitable for a down-shifting material in photovoltaics. This film served multiple purposes: antireflective control for the top cell, light trapping in the Si cell, and absorbing UV and reemitting green light with high quantum yield. Fig. 6b shows the PL spectra (green curve, λ_{ex} = 370 nm) and photoluminescence excitation spectra (black curve, λ_{em} = 517 nm) of (Ba,Sr)$_2$SiO$_4$:Eu^{2+}. The green emission ranges from 460 to 580 nm, and is peaked at 517 nm, corresponding to a Commission Internationale de
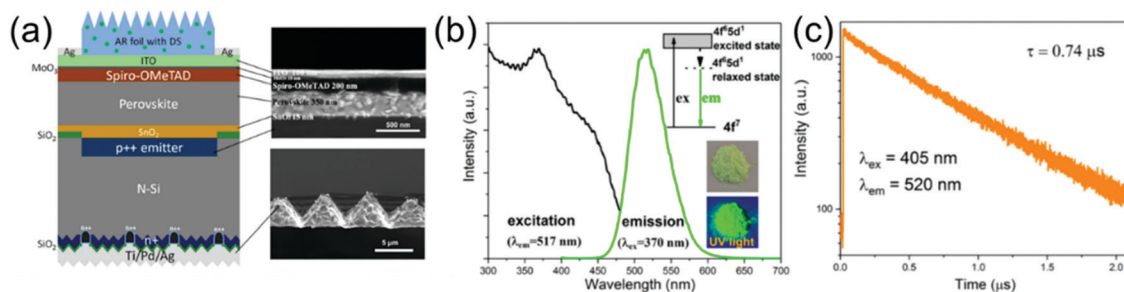
Fig. 6 (a) Schematic illustration of perovskite–silicon homojunction solar cells with a down-shifting AR PDMS layer. Cross-sectional SEM image of the perovskite top cell and the rear textured silicon bottom cell. (b) Excitation and emission spectra of the $(Ba,Sr)_2SiO_4:Eu^{2+}$ phosphor (inset: schematic diagram of the Eu^{2+} 4f–5d transition and photos of phosphor powder under ambient light and UV light (365 nm). (c) Decay curve of the Eu^{2+} emission in the $(Ba,Sr)_2SiO_4:Eu^{2+}$ phosphor.[28]

I'Eclairage (CIE) chromaticity coordinate of (0.1891, 0.6441). The emission of Eu^{2+} ions is due to the transition from the relaxed $4f^65d^1$ state to $4f^7$ ground state. The PL decay curve of $(Ba,Sr)_2SiO_4:Eu^{2+}$ phosphor (λ_{ex} = 405 nm), is detected at 520 nm at room temperature (Fig. 6c). When applied onto a 4 cm^2 monolithic perovskite–silicon TSC, PCE was improved from 20.1% (control device without PDMS layer) to 22.3% (control device with pure PDMS layer) to 23.1% (experimental device with 0.5 wt% $(Ba,Sr)_2SiO_4:Eu^{2+}$ doped PDMS). Moreover, the champion device maintained 90% of the initial performance after 648 h UV exposure at 5 mW cm^{-2}. Catchpole and coworkers also demonstrated a monolithic 2-T perovskite–Si tandem by straightforward integration of PSCs and Si solar cells without an additional layer (Fig. 7a). This interlayer-free device is enabled by highly conductive contact between ALD n-type TiO_2 and P-Si.[29] A possible reason is the substantial density of localized midgap states at the interface between p-Si and TiO_2. These interfacial states can facilitate band to band tunnelling at reverse bias and work as generation–recombination centers at all bias voltages. Electrons move into/out of the defect states *via* local capture/emission and tunnelling in this circumstance. Fig. 7b shows the photovoltaic *J*–*V* performance exhibited by the highest-performing poly-Si tandem cell and the corresponding photovoltaic metrics. The corresponding monolithic 2-T perovskite $(Cs_{0.05}Rb_{0.05}FA_{0.765}MA_{0.135}PbI_{2.55}Br_{0.45})$/SHJ tandems demonstrate an efficiency of 24.1% at reverse scan, with a V_{OC} of 1.763 V, a J_{SC} of 17.8 mA cm^{-2}, and a FF of 78.1%.

2.2.1 Light management of perovskite–silicon TSCs. Light management (LM) is critical for achieving high-performance monolithic 2-T perovskite–silicon TSCs. Si presents a larger optical refractive index than interlayer and perovskite layers, which results in substantial parasitic reflection losses at the internal junction between two subcells. An ideal tandem solar cell usually utilizes surface texture to remove reflection losses by improving light in-coupling and enhance the NIR response at the band edge.

It is possible to position an electrically inert but optically textured layer with an appropriate refractive index directly atop the top contact of TSC to improve light absorption. Albrecht and coworkers employed textured LM foils on the front side of a TSC. The LM foil significantly improved the PCE of the 2-T perovskite-SHJ tandems from 23.4% to 25.5%.[30] Besides, through simulations, they predicted a slightly narrower optimal E_g of the perovskite top sub-cell is needed to match a textured Si device compared with a flat device, and the strong interdependency between E_g and the texture position in the monolithic 2-T device. Their simulations showed that a 32.5% efficiency is realistically achievable with a 1000 nm 1.66 eV-E_g perovskite atop a both-side silicon device. Snaith and coworkers incorporated an optical interlayer consisting of nanocrystalline silicon oxide (nc-SiO_2:H) to mitigate the optical drawback of a flat silicon substrate and increase bottom-cell current density.[31] The 110-nm nc-SiO_2:H interlayer with a refractive index of 2.6 resulted in 1.4 mA cm^{-2} current density gain in the silicon
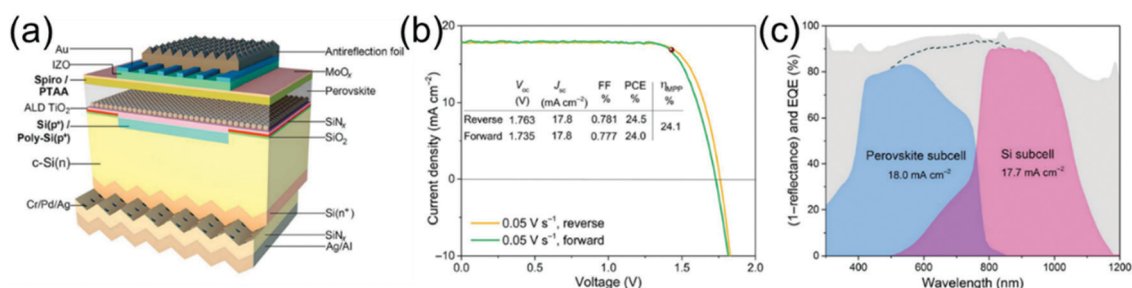

Fig. 7 (a) Scheme of the interlayer-free monolithic perovskite–c-Si tandem solar cell. (b) *J*–*V* curve of the tandem device with both reverse and forward scanning at 0.05 V s^{-1} based on heterojunction poly-Si subcell. (c) Absorbance (1-reflectance) of the tandem device (gray), EQE of the perovskite top cell (blue), and the c-Si bottom subcell (pink).[29]

bottom cell. The anisotropic nature of the nc-SiO$_2$:H interlayer with high transversal and low lateral conductivity supports the further reduction of top-cell shunting *via* shunting quenching. The champion 1 cm^2 monolithic 2-T perovskite–silicon tandem cell exhibits a total current density of 38.7 mA cm^{-2} under AM 1.5G irradiation, and a certified stabilized PCE of 25.2%.

Surface texture can also be realized by using c-Si wafers with μm-sized pyramids. Such a texture improves light in-coupling by minimizing reflections off the front surface while scattering the light within the solar cell to enhance light trapping. However, most monolithic 2-T perovskite–silicon tandems use Si wafers featuring a smooth front side and textured backside to meet the requirement of PSC wet processing. Difficulties of depositing perovskite *via* solution techniques atop μm-sized Si pyramids include uncovered Si pyramids, large shunt paths, and inefficient charge collection. Besides, conventional surface-passivation techniques are incompatible with the rough perovskite surfaces. This configuration, nonetheless, limits light-trapping functions and requires additional anti-reflection foils, the effectiveness of which may be compromised by encapsulation. Moreover, perovskite–silicon tandems with a polished wafer surface have a cost issue, as industrial Si wafers are typically etched and textured on both sides, and chemical-mechanical polishing is cost-prohibitive.

Sargent and coworkers constructed high-performance 2-T perovskite tandems based on fully textured SHJ bottom cells (Fig. 8a).[32] They increased the depletion width by three times at the bases of silicon pyramids to facilitate charge collection in μm-thick perovskites. The J_{SC} of the PSC increases with the thickness of the perovskite layer. The experimental J_{SC} value (certified ∼19.3 mA cm^{-2}) of the ∼1.1 μm-thick perovskite is thereby only within 10% deviation of the theoretical limit (Fig. 8b). As Fig. 8c shows, spectrally weighted reflectance is calculated from the AM 1.5G spectrum at 350–900 nm. They observed that the benefit to reflection began to saturate when the pyramid size was reduced to 2 μm, suggesting the solution-processing techniques of perovskite can be integrated with textured silicon. They also increase carrier diffusion length and suppressed phase segregation by anchoring 1-butanethiol as a self-limiting passivator (SLP) on the perovskite surfaces. The SLP method increases FF from 72% to 77% (Fig. 8d). EQE characterization demonstrates the advantage of switching from a polished front side to a double-side textured architecture (Fig. 8g and h). The introduction of a front texture reduced reflection losses and exhibited efficient light trapping. The device demonstrated a certified PCE of 25.7% and negligible performance loss after the thermal stability test (400 hours, 85 °C) and after MPP tracking (400 hours, 40 °C) (Fig. 8e and f). Huang and coworkers use a blade-coating technique to deposit PSCs' layers on the double-side-textured silicon cells with sub-μm pyramids (Fig. 9).[33] These pyramids with shrunken size are rough enough to scatter light within the silicon relative to large-size pyramids. A N$_2$ knife helps remove solvent vapor, facilitating a quick transition of solution into solid during the blading process (Fig. 9a). When PTAA is spin-coated on a silicon bottom cell, the resulting layer is non-uniform with a thickness of 45 nm in the valleys but a thickness of 8 nm on the pyramids (Fig. 9b). Even with N$_2$-assisted drying, blade coating PTAA at room temperature results in a non-uniform layer (Fig. 9c). When the substrate temperature was elevated to 70 °C, the solvent's accelerated evaporation makes PTAA more uniform on the textured silicon surface (Fig. 9d). The high-throughput blade-coating process can deposit both a conformal hole transport layer and a planarizing perovskite layer that thoroughly covers the textured silicon with increased substrate temperature. This work elongates the path length of long-wavelength light in the silicon and reduced reflection loss to afford 2-T tandems with a J_{SC} >19 mA cm^{-2} and an efficiency of 26.2%.

Note that the bifacial c-Si solar cell and module technology have received considerable attention, which collects light from
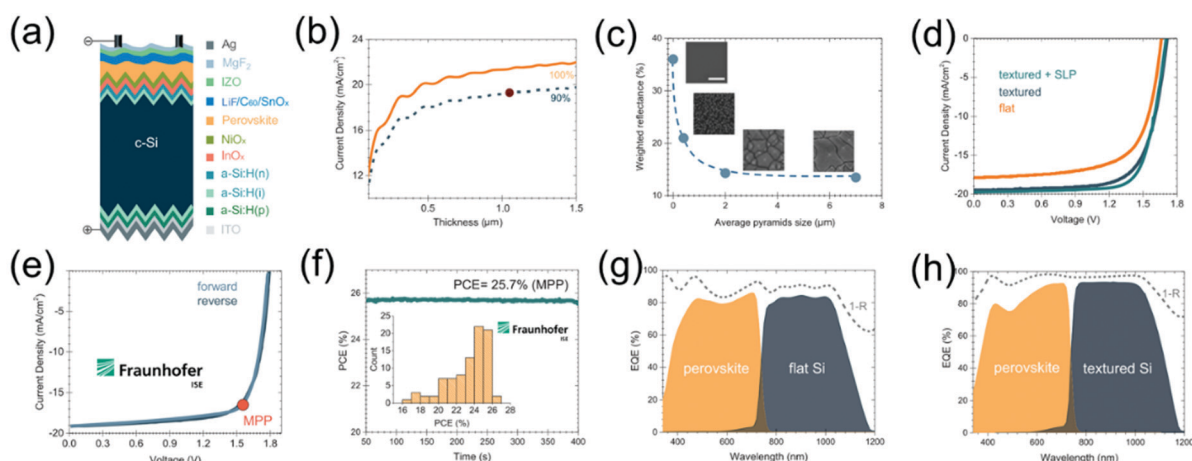

Fig. 8 (a) Structures of solution-processed perovskite–textured silicon tandem. (b) Calculated J_{SC} values of the perovskite cells as a function of perovskite layer thickness. The red dot represents the EQE-integrated J_{SC} value in the textured tandem top cell. (c) Weighted reflectance as a function of c-Si pyramid sizes. The SEM images of different texturing sizes are shown in the insets (scale bar, 2 mm). (d) *J–V* characteristics of flat, textured, and SLP-treated textured tandems. (e) *J–V* curves of certified SLP-treated textured tandems. (f) MPP tracking of certified SLP-treated textured tandems and PCE distributions of 88 individual tandem devices. (g) EQE of the flat devices. (h) EQE of the textured devices.[32]
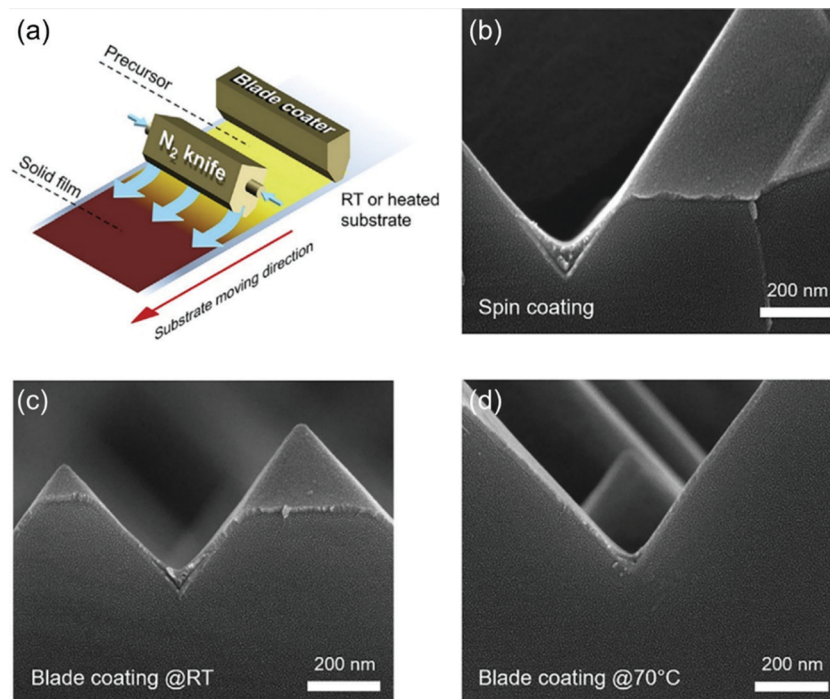
Fig. 9 (a) Scheme of N$_2$-assisted blade coating. (b–d) SEM images of PTAA on textured silicon bottom cells deposited by (b) spin coating, (c) N$_2$-assisted blade coating with the substrate at room temperature, and (d) N$_2$-assisted blade coating with the substrate at 70 °C. The three visible layers are the silicon wafer, ITO front electrode of the silicon cell, and PTAA hole-transport layer.[33]

both the front and rear sides. The bifacial power gain can be up to 50%,[34] and is highly dependent on the albedo of the surroundings and installation geometry.[35] The concept of bifacial cell and module can be naturally transferred to perovskite–c-Si tandems for both 2-T and 4-T configurations.[36–38] In 2021, Sargent, Wolf, and co-workers systematically studied the performance of bifacial 2-T perovskite–c-Si tandems. Because of the additional incident light from the rear side, the optimized E_g of perovskite is reduced to 1.59–1.62 eV. Thus, the bromide content is reduced compared with that in the wide band gap perovskite, which would relax the stability issue coming from the halide segregation.[39]

2.2.2 Bandgap engineering of perovskite–silicon TSCs. The origin of designing tandems is to reduce the thermalization loss. As predicted by the detailed-balanced model, the ideal E_g for the tandem configuration is ∼1.67 to 1.75 eV for the top cell and 1.12 eV for the bottom cell.[40] The 1.12 eV E_g of silicon renders itself a nearly ideal bottom light absorber. Bandgaps from 1.6 to 3.06 eV can be achieved through I/Br and Br/Cl alloying in perovskites. However, wide-E_g alloys in the optimum range for TSCs suffer from short diffusion lengths and photo-induced phase segregation, which lead to poor device performance and large V_{OC} loss. For instance, the replacement of I with Br by >20%, which is necessary to enlarge the E_g to 1.7 eV, results into the formation of I-rich and Br-rich structures under illumination (a process termed the Hoke effect[41]) and limits the Fermi level splitting to that of the lower-bandgap I-rich domains, which effectively act as trap sites. Besides, Br-containing high E_g perovskites exhibited

shorter carrier lifetime than pure I-based perovskite. Compositional tuning of the A and X site in perovskite structures and surface passivation can improve the device performance of high-V_{OC} PSCs.

Cation substitution with Cs or DMA can widen the E_g of perovskite and prevent the large fraction of Br. For instance, the Zhou group reported high-efficiency monolithic 2-T perovskite–Si tandems by tuning the E_g and the optical density of perovskite absorbers.[42] Four different perovskite absorbers (FA$_{0.48}$MA$_{0.37}$Cs$_{0.15}$PbI$_{2.23}$Br$_{0.77}$, FA$_{0.57}$MA$_{0.43}$PbI$_{2.04}$Br$_{0.96}$, FA$_{0.5}$MA$_{0.38}$Cs$_{0.12}$PbI$_{2.04}$Br$_{0.96}$, and FA$_{0.51}$MA$_{0.38}$Cs$_{0.11}$PbI$_{1.85}$Br$_{1.15}$) were adopted to adjust the E_g of perovskite absorbers from 1.65 to 1.72 eV. The FA$_{0.5}$MA$_{0.38}$Cs$_{0.12}$PbI$_{2.04}$Br$_{0.96}$ film presented a much lower trap density of 1.13×10^{16} cm^{-3} than FA$_{0.57}$MA$_{0.43}$PbI$_{2.04}$Br$_{0.96}$ (5.7×10^{16} cm^{-3}), presumably because the small amount of Cs acts as nucleation sites, effectively promotes crystal growth and suppresses defect formation. To maximize the potential of (FA, MA, Cs) PbX$_3$, they optimized the residual PbI$_2$ content in the film, the thickness of the perovskite layer, and the SnO$_2$ electron transport layer. ST-PSCs with a 410 nm FA$_{0.5}$MA$_{0.38}$Cs$_{0.12}$PbI$_{2.04}$Br$_{0.96}$ layer and a transparent MoO$_x$/ITO transparent electrode exhibited an efficiency of 13.09%. The 2-T TSCs based on FA$_{0.5}$MA$_{0.38}$Cs$_{0.12}$PbI$_{2.04}$Br$_{0.96}$ and SHJ delivered a PCE of 22.22% and retained over 85% of their original efficiency after the long-term stability test (500 h).

MAPbCl$_3$ has a wider E_g of 2.88 eV and higher stability than its Br and I counterpart. However, incorporating Cl into perovskite precursor solutions typically cannot increase E_g but increases the perovskite domain size, because the formation and outgassing of MACl alter the crystal nucleation and growth

4548 | *Mater. Chem. Front.*, 2021, **5**, 4538–4564

This journal is © The Royal Society of Chemistry and the Chinese Society 2021

dynamics. Hence, the Cl concentrations in the perovskite film were below the detection limit of energy-dispersive X-ray spectroscopy (EDX) and X-ray photoelectron spectroscopy (XPS), even when a large portion of Cl was incorporated in the precursor solution. McGehee and coworkers alloyed 2–5 mol% $MAPbCl_3$ into the lattice of $FA_{0.75}Cs_{0.25}Pb(I_{0.85}Br_{0.15})_3$,[43] and thereby increased the solid solubility of Cl and the PVSK E_g from 1.63 to >1.67 eV (Fig. 10a). In their work, the Cl to Pb ratio in solid films is increased with the increasing fraction of Cl in the precursor solution, with the grain domain size barely enlarged. Specifically, $Cs_{0.25}FA_{0.75}Pb(I_{0.85}Br_{0.15})_3$:5% $MAPbCl_3$ has a lattice constant of ~6.24 Å, like that of $Cs_{0.25}FA_{0.75}Pb(I_{0.8}Br_{0.2})_3$ and smaller than that of $Cs_{0.25}FA_{0.75}Pb(I_{0.85}Br_{0.15})_3$ (Fig. 10b and f). This is because the lattice constant of the host perovskite was reduced by Cs and Br, making Cl closer to the ideal size for the X-site in the lattice. Consequently, Cl is located in the perovskite lattice and increased E_g, instead of being sacrificed in an MACl volatile phase. The Cl element in the triple-halide films was uniformly distributed through the entire film thickness (Fig. 10c). The bandgap decreases at high Cl content due to double-phase segregation into high Br/Cl phase and high I/Br phase (Fig. 10d–f). The extension from double-halide (I, Br) to triple-halide (I, Cl, Br) significantly increases photocarrier lifetime and charge-carrier mobility and effectively suppresses light-induced phase segregation. This strategy reduced the V_{OC} loss of opaque 1.67 eV-E_g PSCs by 100 mV and boosted the PCE

from ~18% to 20.3%. A PCE of 27.0% and a V_{OC} of 1.886 V were thereby achieved in 1 cm^2 monolithic 2-T tandems by pairing the perovskite top cells with SHJ bottom cells.

The two-dimensional (2D) phase was used to stabilize wide-E_g perovskite, where sheets of $[PbX_6]^{2-}$ octahedra are separated by long-chain or aromatic molecules that act as a passivation agent. For example, n-butylammonium iodide (n-BAI) and phenethylammonium iodide (PEAI) are common 2D additives. Snaith and coworkers introduced n-butylammonium (BA) cations into $(FA_{0.83}Cs_{0.17}Pb(I_yBr_{1-y})_3)$ perovskite. The 2D perovskite platelets were formed and interspersed among highly oriented 3D perovskite grains, suppressing non-radiative charge recombination. The device with an optimal concentration of BA cations exhibited an average stabilized PCE of 17.5 ± 1.3% with a 1.61 eV-E_g perovskite and 15.8 ± 0.8% with a 1.72 eV-E_g perovskite. Unencapsulated devices retained 80% of their post burn-in efficiency after 1000 h in air, while the encapsulated device retained 80% after nearly 4000 h.[44] Shin and coworkers incorporated binary additives, $Pb(SCN)_2$ and $PEA(I_{0.25}SCN_{0.75})$, into 1.68 eV-E_g $(FA_{0.65}MA_{0.2}Cs_{0.15})Pb(I_{0.8}Br_{0.2})_3$ perovskite and thereby delivered a 26.7%-efficiency, stable monolithic 2-T perovskite–Si TSCs.[45] The 2-T devices retained >80% of their initial PCE (20.7%) after 1000 hours of continuous illumination (underneath a sulfur plasma lamp at ~0.8 sun). Anion engineering of phenethylammonium-based 2D additives was critical for controlling the structural and electrical properties of the 2D passivation
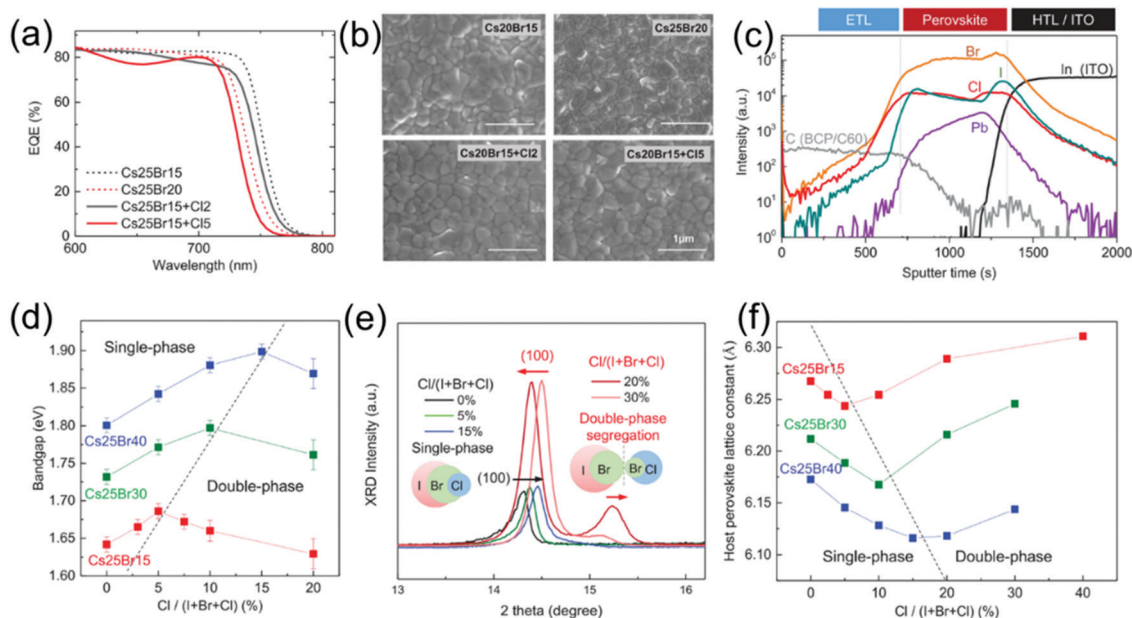

Fig. 10 (a) EQE curves of perovskite with and without Cl. Cs25Br15 and Cs25Br20 refer to $Cs_{0.25}FA_{0.75}Pb(I_{0.85}Br_{0.15})_3$ and $Cs_{0.25}FA_{0.75}Pb(I_{0.8}Br_{0.2})_3$, respectively. Cs25Br15 + Cl2 and Cs25Br15 + Cl5 refer to the triple-halide perovskites with 2 or 5 mol% $MAPbCl_3$ in the Cs25Br15, respectively. (b) Top-view SEM images of double-halide and triple-halide perovskites. (c) The uniform distribution of halides throughout the entire film thickness of the triple-halide perovskite (Cs25Br15 + Cl5). (d) Evolution curves of the band gap for triple-halide perovskite films with an increased ratio of Cl/(I + Br + Cl), based on Cs25Br15 (red), Cs25Br30 (green), and Cs25Br40 (blue), respectively. The dashed line delineates the single-phase and double-phase zones corresponding to bandgap raising and reducing, respectively. (e) Shifting and splitting of the XRD (100) peaks shows the transition from single-phase triple-halide alloy to double-phase segregation in Cs25Br40 with increased Cl content. (f) Curves of host perovskite lattice constant with increasing ratios of Cl/(I + Br + Cl). The dashed line delineates the single-phase and double-phase zones corresponding to band gap increasing and reducing, respectively.[43]

layers bearing a PbI$_2$ framework. Pb(SCN)$_2$ accelerates the growth of 3D perovskite grains. The 2D additive PEA(I$_{0.25}$SCN$_{0.75}$) enables the formation of 2D-phase perovskite both on the surface and at grain boundaries, compared with the sample with Pb(SCN)$_2$ forming only surface 2D phases.

Al-Ashouri and coworkers recently demonstrated a monolithic perovskite–silicon tandem with a certified record-high PCE of 29.15%,[46] surpassing the best silicon single-junction cell (26.7%). The 1.68 eV-E_g perovskite absorber remained phase-stable under illumination through the synergy of fast hole extraction and minimized nonradiative recombination at the hole-selective interface. These features were afforded by a self-assembled, methyl-substituted carbazole monolayer (Me-4PACz) as the hole-selective layer in the PSC. The accelerated hole extraction went along with a low ideal factor of 1.26, a high single-junction FF of 84%, and a high tandem V_{OC} of 1.92 V. In air, the tandem device without encapsulation retained 95% of its initial efficiency after 300 hour of operation.

Because of the series connection feature and the spectral mismatch of solar simulators, it is difficult to measure the photovoltaic properties of 2-T tandem devices. Kim and coworkers designed three-terminal (3-T), monolithic perovskite–Si tandem cells, where the ITO recombination layer was also used as an additional electrode for characterization[47] (Fig. 11a and b). The top subcell was a semi-transparent perovskite solar cell with MAPbI$_3$ as the high-energy absorber, deposited on a flat silicon bottom cell with a textured backside. With the 3-T architecture, the J–V characteristics of each subcell and the tandem cell can be measured independently; the EQE of each subcell can be accurately measured without any light/potential bias or filtration of the probing light. Through optical engineering and bandgap tuning, the best monolithic 3-T perovskite (MAPb(I$_{0.95}$Br$_{0.05}$)$_3$)/SHJ tandem cell exhibits a high PCE of 23.5% and retains 97% of the initial efficiency stored in the dark after 100 days.

The monolithic 2-T perovskite–perovskite–silicon triple-junction solar cells can be a low-cost alternative of III–V semiconductor based triple-junction solar cells, as the latter device requires complicated and costly manufacturing processes. Snaith and coworkers predicted that triple-junctions based on 1.95 and 1.44 eV perovskite subcells and a 1.1 eV silicon bottom cell have an efficiency potential of 38.8%.[48] The Ballif group realized

a proof-of-concept 2-T perovskite–perovskite–silicon triple-junction device by monolithically growing two perovskite cells on double-side textured silicon wafers.[49] They employed an evaporation-spin coating sequential process to deposit the perovskite absorbers, enabling the conformal growth of all the layer stacks directly on the μm-sized pyramids of the Si bottom cell. The triple-junction devices exhibited a V_{OC} of ∼2.7 V, an equivalent cumulative current density of 38.8 mA cm^{-2}, and MPP tracked efficiency of 13.2%.

3. Perovskite–perovskite TSCs

Perovskite–perovskite tandems offer a route to high efficiency and reserve the strengths of low-cost, low-temperature, and low environmental impact fabrication and the possibility of lightweight and flexible form of both subcells. Perovskite has compositional versatility and thus highly adjustable E_g, which offers the potential of realizing high-performance perovskite-perovskite tandems. For instance, the E_g of the Pb-based perovskite can be increased from 1.58 (pure I) to 2.2 eV (pure Br) by substituting I with Br in MAPbI$_3$. The Zhou group pioneered in constructing bottom-up solution-processed 2-T all-perovskite TSCs, where two MAPbI$_3$ subcells are bridged by a spiro-OMeTAD/PEDOT: PSS/PEI/PCBM: PEI charge recombination layer. Despite the low PCE of 7%, this device yields a high V_{OC} of 1.89 V close to the sum of the two MAPbI$_3$ subcells.[50] The Im group fabricated 2-T MAPbBr$_3$-MAPbI$_3$ TSCs by laminating single-junction MAPbBr$_3$ and MAPbI$_3$ planar solar cells.[51] In their work, P3HT and poly[bis(4-phenyl)(2,4,6-trimethylphenyl) amine] (PTAA) hole conductors with Li-TFSI and t-BP additives improved conductivity and reduced charge-transport barriers due to the assistance of the Li/Li$^+$ redox shuttle. Despite the high V_{OC} of 2.25 V, the monolithic 2-T MAPbBr$_3$–MAPbI$_3$ TSCs gave a low J_{SC} of 8.3 mA cm^{-2} and a frustrating sum PCE of 10.8%, suggesting that the combination of only wide-E_g Pb perovskite absorbers fundamentally limits device performance.

The mixed Sn–Pb perovskite presents the bandgap bowing effect, which means the mixed perovskite can present a lower bandgap than those of its Sn-free and Pb-free counterparts. Alloying Pb and Sn in metal halide perovskites can narrow the E_gs down to 1.17 eV for MASn$_{1-x}$Pb$_x$I$_3$ ($x = 0.25$ and 0.5). In principle, the low-E_g Sn–Pb perovskite could be an ideal
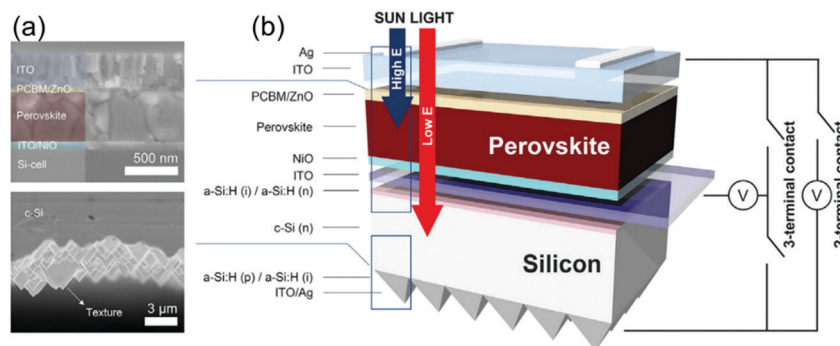

Fig. 11 (a) Cross-sectional FESEM images of perovskite top cell and silicon bottom cell, and (b) schematic illustrations of the monolithic perovskite–Si tandem cell and circuits of the 2,3-T architecture.[47]

candidate as the bottom subcell, opening a pathway for high-performance perovskite–perovskite tandems. Recent optical and device modelling shows that all-perovskite tandems based on 1.22 and 1.80 eV PSCs have a potential to reach 33.4% efficiency with EQE over 90% and V_{OC} of 2.17 eV, rendering this technology potentially competitive with perovskite–Si tandems.[48] To achieve high-performance all-perovskite tandems, low-E_g Sn–Pb perovskite should have a large thickness to harvest sufficient photons, and long carrier diffusion lengths to ensure efficient charge transport and extraction. However, narrow E_g Sn or Sn–Pb PSCs lag far behind wide E_g PSCs currently, which is the major obstacle hindering the advances of all-perovskite tandems. Recently, scientists have carried out composition engineering, additive engineering, solvent engineering, and interface engineering to improve Sn–Pb perovskite based single-junction and tandem devices.

In the early times, devices based on Sn-containing perovskites performed much worse than their pure-Pb counterparts, even though Sn-containing perovskite absorbs a larger fraction of the solar spectrum. Early in 2012, the Shum group invented the first Sn ($CsSnI_3$) PSCs, which delivered a PCE of 0.9%.[52] In 2014, the Kanatzidis group reported that PSCs based on 1.30 eV-E_g $CH_3NH_3SnI_3$ and 1.17 eV-E_g $MASn_{0.75}Pb_{0.25}I_3$ afforded efficiencies of 5.44% and 7.37%, respectively.[53] The disappointing performance of Sn or Sn–Pb based PSCs is associated with both material and device issues. First, Sn and Sn–Pb perovskites have smaller absorption cross-sections than Pb perovskites, which requires a thick-film Sn or Sn–Pb perovskite absorber to achieve high EQE and in turn long carrier diffusion lengths for efficient charge extraction. Second, the Sn-substituted perovskite typically crystallizes more quickly than Pb-based perovskite, resulting in inferior-quality films. Last but not least, the facile oxidation of Sn^{2+} to Sn^{4+} reduces the device performance and stability.

To improve the film quality of Sn-based perovskite, Huang and coworkers reported a simple Pb-assisted two-step spin-coating method. In the control group without PbI_2, a sequential deposition of pure SnI_2 and MAI afforded $MASnI_3$ film with cracks and discontinuous grains.[54] By contrast, the perovskite film is uniform and crack-free with the addition of PbI_2. Therefore, the $MASn_{0.5}Pb_{0.5}I_3$ PSCs achieved a PCE of 13.6% with high reproducibility. Jen and coworkers further improved the performance of low-E_g Sn–Pb PSCs via integrated composition, process, and interface engineering.[55] The solvent-washing methodology with a DMSO-based co-solvent system effectively retards the growth of Sn–Pb perovskites and helps form homogeneous and smooth films by forming the $SnI_2 \cdot DMSO$ intermediate phase. $MAPb_{0.75}Sn_{0.25}I_3$ with ~ 1.35 eV E_g was chosen after the investigation of surface morphology and optoelectronic properties of $MAPb_{1-x}Sn_xI_3$ perovskites with different x values. As the partial substitution of MA with FA stabilizes the Sn–Pb perovskite, the final composition they chose is 1.33 eV E_g $FA_{0.5}MA_{0.5}Pb_{0.75}Sn_{0.25}I_3$. The corresponding devices achieved a PCE of 14.19% and retained >94% of its initial PCE after 30 days in an inert atmosphere. The coupling of the Sn–Pb perovskite bottom subcell (unfiltered: 14.19%, filtered: 5.56%) and a semi-transparent $MAPbI_3$ (13.52%) top subcell endowed the 4-T device with an encouraging PCE of 19.08%.

Via cation and device engineering, Snaith and coworkers demonstrated a 14.8% efficiency for Sn–Pb PSCs. They implemented a technique of precursor-phase antisolvent immersion to deposit uniform $FASn_{0.5}Pb_{0.5}I_3$ film.[56] The mixed solvents of DMSO and DMF with low-vapor pressure retard crystallization via the formation of precursor complexes, followed by an immediate antisolvent bath and gentle heating to crystallize the perovskite. The partial substitution of FA with Cs effectively improved the PCE from 10.9% to 14.1%. The combination of the 1.2 eV Sn–Pb perovskite ($FA_{0.75}Cs_{0.25}Sn_{0.5}Pb_{0.5}I_3$) cell and 1.8 eV E_g perovskite cell ($FA_{0.83}Cs_{0.17}PbI_{0.15}Br_{0.15}$) demonstrates a 17.0%-PCE monolithic 2-T TSC. They also fabricated 20.3% efficiency small-area all-perovskite 4-T tandems based on a semitransparent 1.6-eV E_g $FA_{0.83}Cs_{0.17}Pb(I_{0.83}Br_{0.17})_3$ front cell (filtered: 15.8%) and the $FA_{0.75}Cs_{0.25}Sn_{0.5}Pb_{0.5}I_3$ bottom cell (unfiltered: 14.8%, filtered: 4.5%).

The development of mixed Sn–Pb PSCs can draw lessons from the recent progress of the Pb-free PSCs.[57] First, $FASnI_3$ is more stable than $MASnI_3$ to work as the Sn source. Second, SnF_2 additives are useful for increasing carrier lifetime (by reducing Sn vacancy and background hole density), changing the energetics of the material, and improving the film morphology and stability. Third, hole transporting layers using Li or Co salts as dopants may pose damage to Sn-containing perovskite. Accordingly, Yan and coworkers employed 1.25 eV E_g $(FASnI_3)_{0.6}(MAPbI_3)_{0.4}$ absorber, SnF_2 additives, and a PEDOT:PSS hole transporting layer to fabricate Sn–Pb inverted PSCs. Fig. 12a sketches the steps of forming the precursors for one-step deposition of mixed Sn–Pb perovskite thin fims, consisting of the $FASnI_3$ precursor with the $MAPbI_3$ precursor at different molar ratios. $MAPbI_3$ and $FASnI_3$ films both contain many large grains, yet with some small ones (Fig. 12b and c). As a comparison, the $(FASnI_3)_{0.6}(MAPbI_3)_{0.4}$ film contains relatively smaller but more uniformly distributed grains (Fig. 12d). The device based on $(FASnI_3)_{0.6}(MAPbI_3)_{0.4}$ exhibited a PCE of 15.08% with good reproducibility and negligible hysteresis.[58] The Sn–Pb perovskite exhibits a carrier lifetime of 0.7 ns, much longer than $FASnI_3$ (0.2 ns), but much shorter than $MAPbI_3$ (109 ns). The low-E_g PSCs show relatively low spectral response in the NIR region, which is resulted from the short carrier lifetime (< 20 ns) and the relatively thin (~ 400 nm) Sn–Pb perovskite film. By optimizing the precursor solutions, Yan and coworkers simultaneously increased the grain size, crystallinity, and carrier lifetime to 255 ns at a thickness of 620 nm for the perovskite layer. The low-E_g PSCs achieved a PCE of 17.5%, and a J_{SC} of 28.7 mA cm^{-2} with EQEs of $> 70\%$ in the NIR range.[59] When it was mechanically stacked with a $FA_{0.3}MA_{0.7}PbI_3$ (~ 1.58 eV) front cell, a maximum PCE of 21.2% at reverse scan was demonstrated for the 4-T all-perovskite tandem cell. Yan and coworkers further incorporated 2.5% Cl into $(FASnI_3)_{0.6}(MAPbI_3)_{0.4}$, which simultaneously enlarged the grains, increased crystallinity, and functionalized grain boundaries. Via photothermal deflection spectroscopy (PDS) characterization, they found the incorporation of 2.5% Cl reduced Eu from 27.9 meV (the undoped perovskite device) to 23.9 meV (the experimental device), illustrating that Cl reduced electronic disorder.[60] Transient photocurrent measurement illustrated that
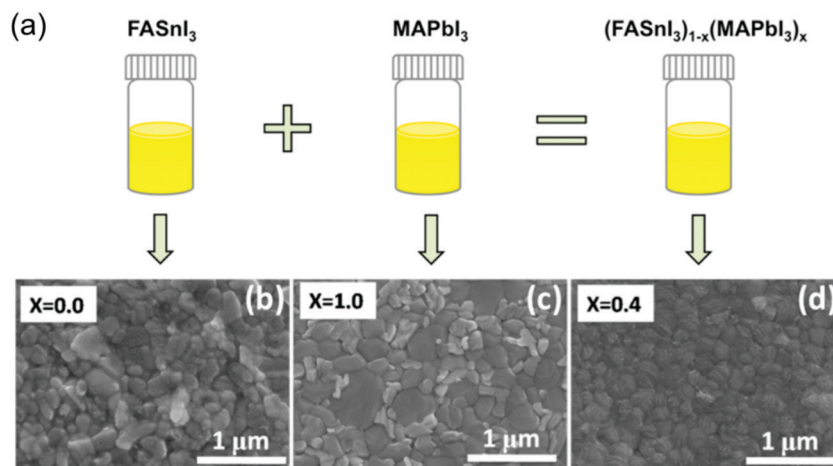
Fig. 12 (a) Scheme of the formation of $(FASnI_3)_{1-x}(MAPbI_3)_x$ precursor. (b–d) SEM images of $(FASnI_3)_{1-x}(MAPbI_3)_x$ perovskite films (x = 0.0, 1.0, and 0.4).[58]

Cl incorporation effectively increased the minority carrier lifetime. The inverted planar Sn–Pb PSCs with ∼750 nm active layer demonstrated a PCE of 18.40%, a V_{OC} of 0.850 V, and a high J_{SC} of 29.31 mA cm^{-2} with negligible J-V hysteresis. By combining this narrow-E_g PSC, wide-E_g $FA_{0.8}Cs_{0.2}Pb(I_{0.7}Br_{0.3})_3$ PSC, and ultra-flat and smooth $Ag/MoO_x/ITO$ ICLs, the monolithic 2-T tandem device achieved PCEs of 21.0% and promising operational stability. Likewise, the incorporation of Br endowed the 1.27 eV Sn–Pb perovskite with a high PCE of 19.1% and a small V_{OC} loss of 0.384 V.[61]

Commonly used Sn-based narrow-E_g perovskite has shorter carrier diffusion lengths and lower absorption coefficient than the Pb-based perovskite. In Sn-containing PSCs, electrons exhibited much shorter diffusion length than holes. Huang and coworkers incorporated 0.03 mol% cadmium ions (Cd^{2+}) into $FA_{0.5}MA_{0.45}Cs_{0.05}Pb_{0.5}Sn_{0.5}I_3$ perovskite to de-dope Sn–Pb perovskite and reduce the electron trap density, which effectively enhances the recombination lifetime, electron mobility, and electron diffusion length.[62] With this strategy, the optimized perovskite thickness is increased from 620 to 1000 nm to yield stabilized efficiencies of 20.2% for single-junction 1.22 eV Sn–Pb PSCs. When 1.80 eV $FA_{0.6}Cs_{0.4}Pb(I_{0.65}Br_{0.35})_3$ PSCs and the 1.22 eV Sn–Pb PSCs are combined, the best 2-T tandem devices achieve a high PCE of 23.0% under reverse scan, with a V_{OC} of 1.99 V, a J_{SC} of 15.1 mA cm^{-2}, and FF of 77%.

Via a comproportionation reaction, Tan and coworkers reduced Sn^{4+} to Sn^{2+} by doping metallic Sn into mixed Sn–Pb perovskite solution.[63] When Sn^{4+} free precursor solution is processed, the formation of Sn vacancies caused by Sn^{4+} in the precursor solution can be suppressed in perovskite films (Fig. 13a). Thereby, the Sn vacancies in the grains were reduced, and a 3 μm long carrier diffusion length was achieved in mixed Sn–Pb perovskite. They obtained a PCE of 21.1%, along with FF > 80% and J_{SC} > 32 mAcm^{-2} for a 1.22 eV Sn–Pb perovskite. They fabricated monolithic all-perovskite TSCs using a 1.77 eV-E_g front subcell and a 1.22 eV back subcell (Fig. 13b). The 2-T TSCs delivered a certain PCE of 24.8% for a 0.049 cm^2 device, with a high V_{OC} of 1.965 V, a J_{SC} of 15.6 mA cm^{-2}

and a high FF of 81%, and retained 90% of their initial performance after 463 hour MPP operation under simulated 1 sun illumination (Fig. 13c and d). The Tan group recently used the surface-anchoring zwitterionic antioxidant to inhibit Sn^{2+} oxidation and passivate defects at the surfaces and grain boundaries. Thereby they fabricated 21.7%-efficiency narrow-E_g single-junction solar cells, and obtained certified 24.2%-efficiency 1 cm^2-area all-perovskite tandem cells. The encapsulated tandem devices retained 88% of their initial PCE after 500 hours' operation under 1 sun illumination under ambient conditions.[64]

Zhu and coworkers incorporated 7% guanidinium thiocyanate (GuaSCN) to improve the structural and optoelectronic properties of the 1.25 eV Sn–Pb perovskite absorber (($FASnI_3)_{0.6}$ ($MAPbI_3)_{0.4}$).[65] On the one hand, SCN ions with a reasonable amount enlarged the grain size and reduced pinholes. On the other hand, Gua with a large ionic radius separated the original 3D ABX_3 perovskite and implemented the 2D–3D heterojunction. The 2D structures passivate surface and grain boundaries through its wider bandgap, block the diffusion of oxygen into grains; and prevent Sn from diffusion out of grains. Consequently, GuaSCN reduced defect densities by a factor of 10; extended carrier lifetimes to 1232 ns; elongated the carrier diffusion length to 2.5 μm; and reduced the surface recombination velocity to 1.0 × 10^2 cm s^{-1}. These improvements endowed $(FASnI_3)_{0.6}(MAPbI_3)_{0.4}$ with >20% efficiency. The combination of low-E_g and wide-E_g PSCs makes 25.0%-efficiency 4-T and 23.1%-efficiency 2-T all-perovskite TSCs.

4. Perovskite−CIGS TSCs

Apart from perovskite–c-Si and perovskite–perovskite tandem cells discussed above, a perovskite cell can also be integrated with a CIGS cell, which has the optimal E_g of 1.08–1.15 eV for the high-performance single-junction device.[66] CIGs have a large absorption coefficient (10^5 cm^{-1}) and highly tunable E_g from 1.00 to 1.70 eV by tuning the ratio of Ga/In. Besides, the CIGS technology is rapidly growing with mature commercial
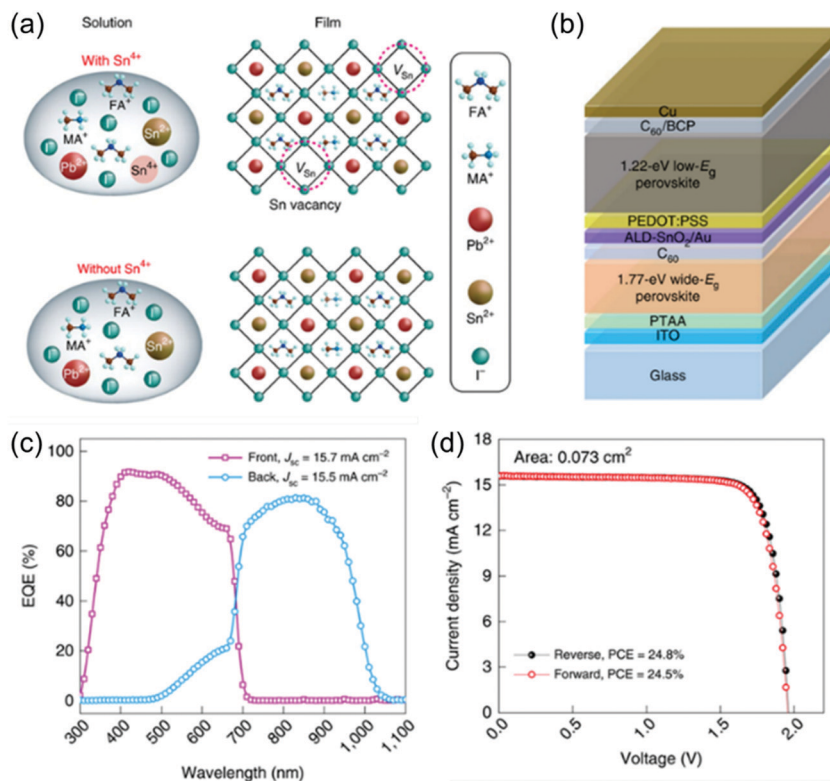
Fig. 13 (a) Scheme of the formation of Sn vacancies in mixed Sn–Pb perovskite due to the presence of Sn^{4+} in the precursor solution and the suppression of Sn vacancy formation because of the absence of Sn^{4+}. (b) The device architecture of the perovskite–perovskite tandem solar cell. (c) EQE curves of the front (15.7 mA cm^{-2}) and back (15.5 mA cm^{-2}) subcells. (d) J–V curves of the tandem solar cell (0.049 cm^2).[63]

thin-film products. These demonstrated the great potential of perovskite–CIGS TSCs, considering easier processing, flexible form factor, and light weight, *etc.* The requirement of perovskite bandgap in this TSC is generally similar to perovskite–Si tandems.

4.1   Perovskite–CIGS 4-T TSCs

Perovskite–CIGS 4-T tandems do not need to match the current density, and both subcells can easily work at the MPP point. In the 4-T configuration, ST-PSCs can freely choose the n–i–p or p–i–n structure. Transparent electrodes for semi-transparent PSCs are carefully summarized in the section of perovskite–Si 4-T tandems and do not need emphases in this section. PSCs can have superstrate (light enters the devices from the substrate) and substrate configuration (light enters from the film side) (Fig. 14). The superstrate configuration limits the choice of the substrate to transparent materials. In the substrate configuration, perovskite can be grown on substrates like flexible polymer films and other metal foils. The substrate configuration can facilitate processing directly on CIGS solar cells to realize high-performance polycrystalline all-thin-film tandem devices. However, the substrate architecture constrains device processing and the electronic quality of the perovskite absorber and interlayer. Tiwari and coworkers reported 16.1%-efficiency substrate-configuration ST-PSCs with an architecture of substrate/In$_2$O$_3$:H/PTAA/MAPbI$_3$/PCBM/ZnO NPs/ZnO:Al/ Ni-Al grid.[67] F4-TCNQ-doped PTAA and PCBM ensure efficient

charge extraction and transport, and the ZnO NPs can reduce the sputtering damage and provide suitable band alignment with sputtered ZnO:Al. The semitransparent PSC exhibits a high AVT of 80.4% between 800 and 1200 nm, allowing the realization of tandem devices with sum PCE of 22.1% and 20.9% for CIGS (unfiltered: 19.2%, filtered: 6.0%) and CuInSe$_2$ (unfiltered: 13.0%, filtered: 4.8%) bottom cells, respectively.

Mathews and coworkers used triple cation perovskite to demonstrate a 16% efficiency ST-PSCs, which had an average transmittance of 12% in the visible region and >50% in the NIR region, respectively. They observed that the Ag buffer layer improved the adhesion to the underlayer and FF, outcompeting the MoO$_x$ buffer layer. They demonstrated a 20.7% efficiency for 4-T tandem based on the ST-PSCs and CIGS (unfiltered: 12.3%, filtered: 4.7%).[70] Catchpole and coworkers engineered the perovskite composition: FA is the primary cation (75%) due to its stability towards moisture and heat; 15% MA can reduce the size discrepancy of FA and Cs, reduce defects, and facilitate the formation of α-phase perovskite. Cs can inhibit humidity-induced decomposition and strain-induced phase segregation, remove the yellow phase, and improve device performance and stability. Rb can balance the tolerance factor, and enhance efficiency and stability. Consequently, they utilized the 1.62 eV E_g Cs$_{0.05}$Rb$_{0.05}$FA$_{0.765}$MA$_{0.135}$PbI$_{2.55}$Br$_{0.45}$ and developed a 18.1%-efficiency ST-PSC. The combination of ST-PSC and CIGS subcell (unfiltered: 16.5%, filtered: 5.8%) gave a 4-T tandem efficiency of 23.9%. They also delivered a 16.0% PCE ST-PSCs
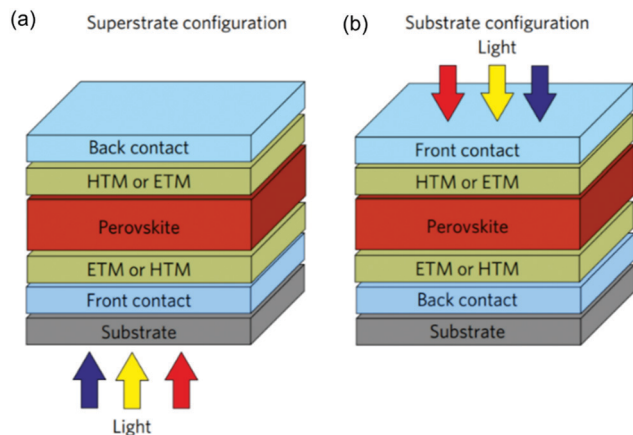
Fig. 14 Scheme of a perovskite solar cell in the (a) conventional superstrate configuration and (b) the substrate configuration.[67]

based on 1.75 eV $Cs_{0.1}Rb_{0.05}FA_{0.75}MA_{0.15}PbI_{1.8}Br_{1.2}$, and 23.4% 4-T perovskite–CIGS tandem based on 16.0%-efficiency ST-PSCs and CIGS. Besides, the four-cation perovskite absorbers exhibit less oxygen sensitivity than $MAPbI_3$. They deduced that the interaction between MA and oxygen molecules increased surface recombination, resulting in oxygen-induced degradation.

For perovskite–CIGS 4-T tandems, it is essential to reduce the defect density and increase the long lifetime of wide-E_g perovskite films. In 2015, Tiwari and coworkers updated the performance of perovskite–CIGS 4-T tandems through concerted efforts.[68] On the one hand, PCBM was incorporated into the regular device structure, enabled by a hybrid thermal evaporation-spin coating technique. PCBM facilitated the growth of high-quality perovskite absorbers and inhibited hysteresis. Fig. 15a and b presents the cross-sectional SEM images of the planar PSCs with and without the PCBM layer, respectively. The perovskite layer on ZnO exhibits considerable surface roughness and thickness non-uniformity. When grown on PCBM, a uniform and compact perovskite layer with a large grain size can be obtained. As Fig. 15c and d shows, the device with a PCBM layer exhibits a PCE of 14.5%, together with a V_{OC} of 1.101 V, J_{SC} of 17.6 mA cm^{-2}, and FF of 74.9%. On the other hand, sputtered In_2O_3:H is employed as a transparent rear electrode, yielding 14.2% steady-state efficiency, and 72% average transmittance between 800 and 1150 nm (Fig. 15e and f). Furthermore, they demonstrated 20.5% efficiency for the 4-T perovskite–CIGS (unfiltered: 18.3%; filtered: 6.3%) tandem configuration. *Via* the 2D–3D heterostructure strategy, Zhu and coworkers from the NERL demonstrated ~20%-efficiency opaque PSCs by incorporating PEAI and $Pb(SCN)_2$
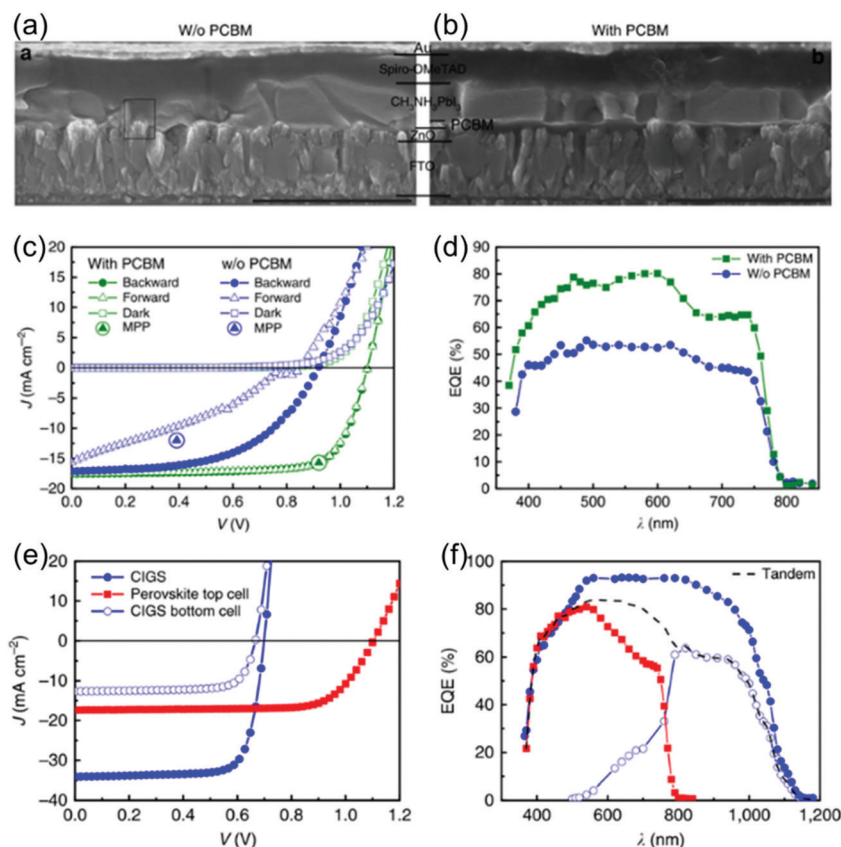

Fig. 15 The cross-sectional SEM images of devices without (a) and with (b) PCBM, respectively. The current density–voltage (J–V) curves (c) and EQE spectra (d) of the planar perovskite solar cells. The current density–voltage (J–V) curves (e) and EQE spectra (f) of the four-terminal perovskite–CIGS tandem device.[68]

binary additives in the $FA_{0.65}MA_{0.20}Cs_{0.15}PbI_{2.4}I_{0.6}$ precursor.[71] These additives form a quasi-2D phase located primarily at grain boundaries. The synergy of PEA^+ and SCN^- overcame the separate challenges of each additive, enhanced perovskite morphology, inhibited PbI_2 formation (compared with the sole addition of $Pb(SCN)_2$), and reduced defect density and energetic disorder. The coupling of a 1.68 eV ST-PSC (17.1% efficiency) and a 1.12 eV CIGS bottom cell (unfiltered: 20.7%; filtered: 8.8%) afforded a record-high 25.9%-efficiency 4-T polycrystalline perovskite–CIGS 4-T TSCs.

Segawa and coworkers achieved a high PCE of 28% in a perovskite–CIGS 4-T tandem comprising a perovskite top cell and a CIGS bottom cell with E_g of 1.59 and 1.02 eV, based on a spectrum splitting system equipped with a dichroic mirror with splitting wavelengths of 775 nm. Tandem devices using perovskite and CIGS can potentially exhibit high flexibilities, which cannot be achieved with Si cells. Spectrum splitting tandem cells may not be ideal for practical applications. Nonetheless, this study shows experimentally that perovskite–CIGS TSCs are not only mechanically superior but also exhibit a higher efficiency than Si-based TSCs.[72,73]

4.2 Perovskite–CIGS 2-T TSCs

Different from other tandems, only p–i–n PSCs can work as top cells for perovskite–CIGS 2-T tandems, as the bottom CIGS cell has a typical structure of a glass/Mo/p-CIGS/n-CdS/ZnO structure. In 2015, Guha and coworkers realized monolithic 2-T perovskite–CIGS tandems, where both subcells are customized (Fig. 16).[69] The E_g of CIGS was narrowed from 1.1 eV to 1.04 eV. The optical properties of perovskite were controlled by vapor-based halide exchange reactions. They designed a reactor for continuous in situ monitoring and

precise control of perovskite's E_g via vapor-based halide exchange reactions (Fig. 16a). The sample of spin-coated PbI_2 was annealed by the excess solid MAI vapor source until the layer is converted to 1.58 eV perovskite. MAI can be replaced with MABr. With continued annealing, the E_g will increase when I is replaced by Br, and the samples exhibited different Eg values: 1.65 eV (B2), 1.72 eV (B3), and 1.75 eV (B4). In a reverse-sequence process, the E_g of a pure bromide perovskite (C1 with 2.29 eV E_g) is reduced to the following values of 1.95 eV (C2), 1.86 eV(C3), and 1.7 eV (C4) with the MAI vapor (Fig. 16b and c). Consequently, a PCE of 10.9% was obtained for a monolithic 2-T perovskite–CIGS tandem cell (Fig. 16d).

Besides, CIGS has a very rough surface due to the common vacuum fabrication (sputtering and co-evaporation), which is problematic for building a smooth ICL atop it and may cause the failure of PSCs. Albrecht and coworkers introduced two new hole-selective contacts (MeO-2PACz and 2PACz) for p–i–n PSCs.[74] These two molecules feature carbazole blocks with phosphonic acid anchoring groups, which enabled the formation of self-assembled monolayers (SAMS) on various oxides, which is ordered and stabilized by π–π interactions between adjacent carbazole fragments. These two SAMS exhibit weaker absorption in the visible wavelength compared with the PTAA interlayer and have an energy alignment to the perovskite absorber. The MeO-2PACz SAM layer enabled dopant-, additive- and interlayer-free PSCs with stabilized PCEs of up to 21.1%, and allowed the realization of a monolithic 2-T CIGSe/ perovskite TSC with a certified PCE of 23.26%. The simplicity and diverse substrate compatibility of SAMs help ease the fabrication of 2-T CIGSe/perovskite TSC. Yang and coworkers designed a 22.43% efficiency 2-T perovskite–CIGS tandem with an architecture of Glass/Mo/CIGS/CdS/i-ZnO/boron-doped ZnO
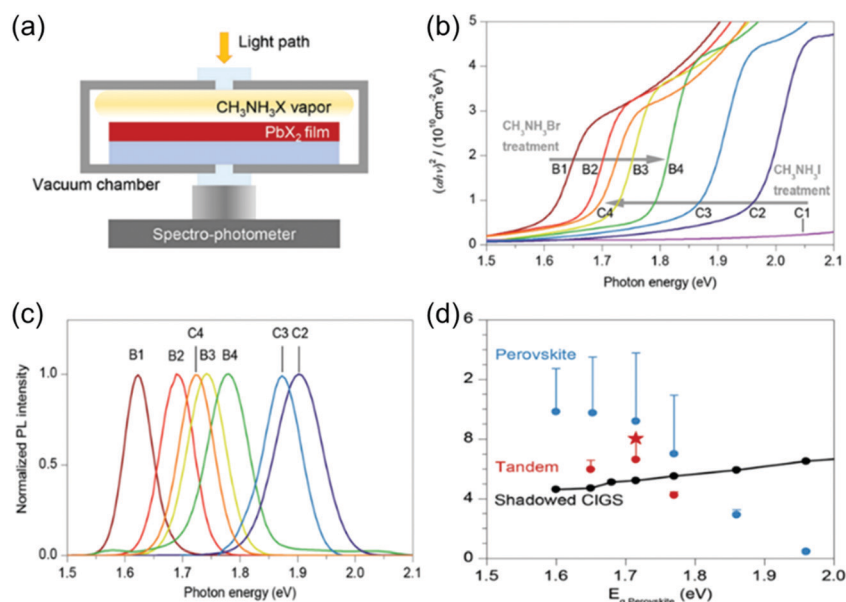

Fig. 16 (a) Scheme of in situ bandgap tuning apparatus. (b) Tauc plots of sample series B and C, showing a blueshift progression with CH_3NH_3Br vapor treatment and a redshift progression with CH_3NH_3I vapor treatment, respectively. (c) PL spectra of series B and C. (d) Efficiency plotted against the bandgap of perovskite.[69]

(BZO)/ITO/PTAA/Perovskite-PCBM/ZnO NPs/ITO/MgF$_2$. They carried out nanoscale interface engineering of the CIGS surface and used a heavily doped PTAA HTL between two subcells that preserved V_{OC} and enhanced FF and J_{SC}.[75] They first deposited an ITO layer and then used chemical mechanical polishing to smooth out the ITO surface. The polishing process reduced the vertical distance of ITO to 40 nm. Note, that the BZO layer under the ITO was not polished, and the original CIGS solar cell can be retained. As the BZO layer displayed a much lower work function (4.0 eV) than PTAA (5.1 eV), the ITO between BZO and PTAA created better ohmic contact. A monolithic 2-T perovskite–CIGS TSC achieved a 22.43% efficiency, and the unencapsulated devices in air retained 88% of their initial efficiency after 500 hours of aging under continuous 1 sun illumination.

4.3 Perovskite–CZTSSe TSCs

Compared with CIGS, Cu$_2$ZnSn(S,Se)$_4$ (CZTSSe) does not use rare metal elements, In and Ga, and thus has a low cost. CZTSSe has a high absorption coefficient of $>10^4$ cm^{-1} in the visible wavelengths and a high theoretical PCE of 28%. The E_g of CZTSSe can vary from 1.00 to 1.50 eV, which is mainly tuned by the ratio of S/Se.

Guha and coworkers demonstrated a monolithic 2-T tandem cell with solution-processed kesterite CZTSSe and MAPbI$_3$. The device exhibited a high V_{OC} of 1.353 V, close to the sum V_{OC} of the single-junction subcells. The 2-T tandem exhibited a very disappointing PCE of 4.6%, compared with 11.6% for CZTSSe and 12.3% for MAPbI$_3$.[76] Although other factors to the high Rs (15.7 Ω cm^2) cannot be ruled out, the drastically reduced illumination in all layers and high Rs of the Al contact are major contributors to the low J_{SC} and FF. Ding and coworkers present a tandem combining solution-processed perovskite and CZTSSe subcells in a reflective configuration.[77] The 1.70 eV-E_g perovskite subcell acts as a spectral filter reflecting the sub-bandgap photons to a low bandgap CZTSSe cell. A 4-T measurement afforded a sum efficiency of 16.1%, showing the potential of perovskite–CZTSSe 4-T tandems in realizing high performance and low fabrication cost simultaneously.

5. Perovskite–organic TSCs

Organic solar cells (OSCs) are another emerging PV technology.[78,79] OSCs can be fabricated through low-cost solution processes using environmentally friendly materials. OSCs can be made into lightweight, flexible, and semi-transparent devices. Currently, OSCs have achieved up to 18.2% certified PCE.[80] Perovskite and organic semiconductors have composition and molecular tunability to enable a large pool of photoactive material with different optoelectronic properties, offering the feasibility to construct high-performance perovskite–organic TSCs.

5.1 Perovskite–organic 4-T TSCs

Hygroscopicity risk and easy decomposition are the obvious drawbacks of organic–inorganic hybrid perovskites. Compared with the hybrid organic–inorganic perovskites, all-inorganic

perovskite solar cells display better stability toward moisture, light soaking, and thermal stressing.[81,82] In particular, CsPbI$_3$ perovskite with E_g of 1.73 eV can serve as a top cell in tandem devices with silicon solar cells. CsPbI$_3$ also exhibits good thermal stability. However, it is difficult to maintain the bandgap and phase stability of CsPbI$_3$, due to their low tolerance factor, the large crystal distortion, and moisture. The all-inorganic perovskite CsPbBr$_3$ has demonstrated the most promising stability against heat and humidity. For instance, the CsPbBr$_3$-based mesoporous PSCs displayed minimal performance degradation when exposed to highly humid air and extreme temperatures for longer than 3 months. CsPbBr$_3$ presents a wide E_g of ≈ 2.3 eV, efficiently harvests short-wavelength sunlight in the 300–530 nm wavelength range, and can achieve $\approx 90\%$ EQE at the wavelength ≈ 400 nm. Generally, a high V_{OC} of ≈ 1.25 V and high transmittance in the visible region at wavelengths >530 nm can be afforded by mesoporous CsPbBr$_3$ PSCs, indicating the potential of CsPbBr$_3$ in the ST device and TSCs. Li and coworkers addressed OSCs' photostability issue without efficiency loss by constructing CsPbBr$_3$/organic 4-T TSCs. They prepared high-quality CsPbBr$_3$ all-inorganic perovskite films with a low defect concentration using the dual-source vacuum thermal evaporation method. The corresponding CsPbBr$_3$ film displays a high AVT of 90.9% in the 530–800 nm wavelength range. The opaque planar PSC exhibited a V_{OC} of 1.44 V, a PCE of 7.78%, and good UV stability. The semitransparent PSC with the transfer-laminated PH1000 anode showed a PCE of 5.98% with a J_{SC} of 6.15 mA cm^{-2}, a V_{OC} of 1.38 V, and an FF of 70.51%. The perovskite ST devices were paired with PTB7-Th:PC$_{71}$BM (unfiltered: 9.06%, filtered: 4.63%), PBDB-T:ITIC (unfiltered: 10.10%, filtered: 5.59%) and PBDB-T-SF:IT-4F (unfiltered: 13.72%, filtered: 8.05%) systems, to deliver a sum PCE of 10.61%, 11.57%, and 14.03%, respectively. These tandems exhibit good UV stability, which is reflected in the fact that they reserve 97.3–99.4% of the initial PCEs after 100 mW cm^{-2} for 120 h.[83]

5.2 Perovskite–organic 2-T TSCs

The study of perovskite–organic TSCs was pioneered by thre Yang group in 2015. In their work, MAPbI$_3$ was processed *via* a one-step deposition with a small-molecule additive named BmPyPhB, which provided heterogeneous nucleation sites and improved the uniformity of the initial nucleation process of perovskite crystals. The organic system (PBSeDTEG8:PCBM) exhibited photosensitivity up to 950 nm and good thermal stability to endure PSC's thermal annealing process. The monolithic 2-T perovskite–organic tandem cells exhibit an efficiency of 10.2%.[84]

The Jen group demonstrated unique semi-transparent monolithic 2-T TSCs by rationally choosing selective absorbing photoactive materials.[85] They developed 2.36 eV-E_g FAPbBr$_{2.43}$Cl$_{0.57}$ perovskite with efficient selective absorption in the UV region and meanwhile utilized an organic BHJ blend of PTB7-Th:6TIC-4F with an absorption onset at ≈ 980 nm (Fig. 17a). Therefore, the balance of energy loss between thermalization
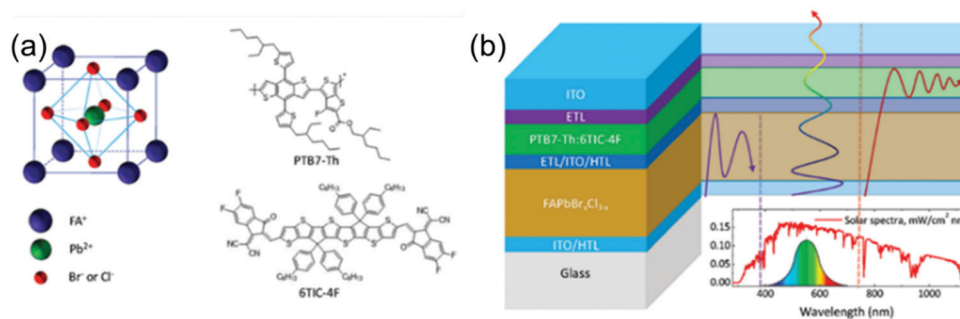
Fig. 17 (a) Scheme of $FAPbBr_xCl_{3-x}$ perovskite crystal lattice, Chemical structures of PTB7-Th and 6TIC-4F. (b) Device architectures of selective absorbing tandem ST-PVs.[85]

and transmission is improved, and the resulting 2-T S-T TSC delivered a PCE of 10.7%, an averaged transmittance of 52.91%, and a light utilization efficiency of 5.66% (Fig. 17b). The Jen group further employed phenmethylammonium bromide (PMABr) to passivate the wide-E_g perovskite $Cs_{0.1}(FA_{0.6}MA_{0.4})_{0.9}$ $Pb(I_{0.6}Br_{0.4})_3$ and obtain a high V_{OC} of 1.22 V for the PSC.[86] The assembled rigid perovskite–organic 2-T TSCs yielded a remarkable PCE of 15.13%, with V_{OC} of 1.85 V, J_{SC} of 11.52 mA cm^{-2}, and FF of 70.98%. Moreover, they realized flexible perovskite–organic TSCs with a PCE of 13.61% and a V_{OC} of 1.80 V. The rigid and flexible perovskite–organic TSC generated a solar-to-hydrogen efficiency of 12.30% and 11.21%, illustrating the potential application of perovskite–organic TSCs in a photovoltaics-driven water splitting system. Zeng *et al.* demonstrated all-inorganic perovskite–organic TSCs with a $CsPbI_2Br$ cell as the front cell and PTB7-Th:CO_i8DFIC:$PC_{71}BM$ as the rear cell. The wide-E_g $CsPbI_2Br$ can absorb short-wavelength photons before 650 nm, while the low-bandgap NFA CO_i8DFIC can absorb long-wavelength photons until 1050 nm. They uses a device structure of ITO/SnO_2/ $CsPbI_2Br$/PTAA/ICL/ZnO/PTB7-Th:CO_i8DFIC:$PC_{71}BM$/MoO_3/Ag,

where the ICL consisting of MoO_3/Au was made by thermal deposition. The corresponding best tandem exhibits a PCE of 15.04%, with a V_{OC} of 1.71 V, a J_{SC} of 11.98 mA cm^{-2}, and an FF of 73.4%.[87] Very recently, Chen *et al.* developed a semi-empirical model to calculate the practical PCE limits of perovskite–organic TSCs. Based on their calculation, an efficiency >30% is approachable with the rapid advances of low-E_g organic semiconductors and wide-E_g perovskite materials. They prepared monolithic perovskite–organic TSCs by employing a 1.77 eV-E_g $FA_{0.8}$ $MA_{0.02}Cs_{0.18}PbI_{1.8}Br_{1.2}$ for the front cell and a 1.41 eV-E_g organic material for the rear subcell (Fig. 18a).[88] As shown in Fig. 18b, the absorbed energy distribution is simulated by the transfer matrix method. To effectively match the J_{SC}, they established the relationship between the photo-current and the thickness of each subcell. The highlighted blue curve indicates that the J_{SC} of both subcells is matched theoretically (Fig. 18d). Featuring all-thermally evaporated BCP/Ag/MoO_3 ICLs, the 2-T monolithic perovskite–organic tandems delivered good reproducibility and a landmark PCE of 20.6% (certified as 19.54%). The UV sensitivity of OPVs is significantly reduced with the UV
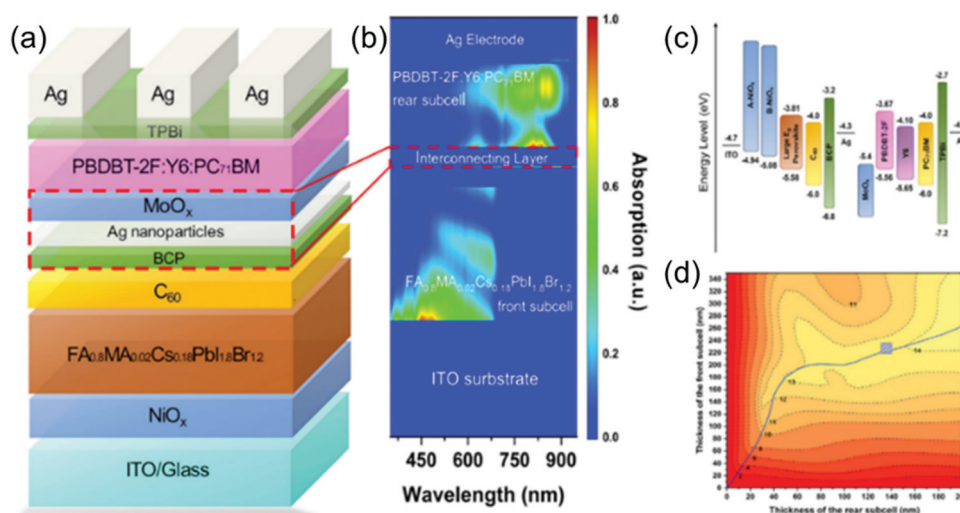

Fig. 18 (a) Perovskite–organic tandem structure with an ICL of MoO_x/Ag nanoparticles/BCP. (b) The simulation of the photon absorption distribution in tandem. (c) Energy level distribution of the components in the tandem device. (d) Stimulated current density as a function of the thicknesses of the front and rear subcells.[88]

filtering function of the perovskite layer. Recently, the integrated perovskite–organic solar cells without any recombination layers have generated wide attention. This integrated structure takes the advantages of tandem cells using both perovskite solar cells and NIR BHJ organic solar cells for wide-range absorption and the simple fabrication of a single-junction device.[89–91] The high V_{OC} and wide-range absorption can be maintained at the same time. However, as this device does not belong to the tandem device in the strict sense, it will not be discussed here.

Conclusions and outlook

Perovskite solar cells are an ideal candidate to construct tandem cells, due to their high V_{OC}, highly tunable E_g, and low-temperature solution processability. We have presented the key advances of perovskite–silicon, all-perovskite, perovskite–CIGS, and perovskite–organic TSCs. Currently, the 1 cm^2 perovskite–silicon monolithic two-junction, the two-terminal device has achieved the highest results of 29.15%, which pushes further beyond the highest efficiency for a single-junction silicon cell with a 9% relative advantage. Perovskite TSCs are stepping towards commercialization, which requires high device efficiencies, long-term stability, and low-cost and reproducible fabrication. The following challenges and strategies should be considered for future developments.

The high-performing tandems required reduced additional optical losses (reflective losses and parasitic absorption losses) and electrical losses in a tandem structure. The optical losses of PSCs are greatly reduced by changing the configuration of PSCs from n–i–p to p–i–n, which may account for the phenomenon that the maximum efficiency of TSCs is obtained with p–i–n PSCs. The parasitic absorption in p–i–n PSCs can be minimized by reducing the thickness of the electron transport layer like C_{60} and PCBM, where the following wide-bandgap BCP/Bphen layer can work as the hole-blocking layer and the buffer layer. Take perovskite–Si TSCs as an example, PSCs with the p–i–n structure are the most promising for high PCEs due to the less optical losses, low cost, and compatible fabrication process with the SHJ structure.[92]

LM layers like MgF_2 and SiO_x on the substrate surface should be utilized to reduce the reflective optical loss. The transparent electrode should have high conductivity and high transparency. ICLs should have small resistance and lateral conductivity and high transparency. The high-performance tandems also require efficient subcells.

(1) Wide-bandgap PSCs

Compositional engineering, the partial substitution of I by Br for instance, can enlarge the bandgap of perovskite. The quality of wide-bandgap perovskite film should be improved, with low defect concentration, weak charge recombination, and long carrier lifetime. As discussed above, many strategies are reported, such as the incorporation of Gua/PEA-based additives for constructing the 2D–3D hybrid structure, Lewis bases/acids, PbI_2, Br and Cl, ligand passivation, and metal ions. To fabricate

PSCs on the textured or rough surfaces of Si and CIG solar cells, some special fabrication methods should be utilized, like blade-coating, thermal co-evaporation, and the vacuum-solution binary step.

(2) Narrow-bandgap bottom cells

The Sn–Pb PSCs should be improved by tackling the material and device issues. First, Sn and Sn–Pb perovskites require thick film perovskite absorbers and in turn long carrier diffusion lengths. Second, the quick crystallization of Sn-substituted perovskite results in inferior-quality films. Last, the facile oxidation of Sn^{2+} to Sn^{4+} degrades its device performance. Several strategies are reported and summarized in the manuscript, which is partially similar to the strategies for wide-E_g perovskites, such as the addition of Cl, excess metal ions, SnI_2, SnF_2, $SnCl_2$, FA, Cd, insulating polymers, and alkali metal ions. For organic bottom cells, high-performance non-fullerene acceptors, especially fused-ring electron acceptors, should be developed. The match of donors and acceptors should be guaranteed. The ternary/multiple strategies can be applied. The bulk-heterojunction active layer should be optimized by device engineering, including solvent additive, thermal annealing, and solvent vapor annealing. As Si and CIG bottom cells already have very mature products, their improvement is not the highlight to some extent. The bandgap and thickness of the top and bottom cells should be prudently optimized together.

To reduce the cell-to-module PCE gap, the main step is to obtain high-performance large-scale perovskite top cells. Our group recently performed systematic investigations on fabricating PSCs *via* blade coating under ambient conditions with high humidity and room temperature. The morphological and photoluminescence characterization indicate that air-knife-assisted drying significantly contributed to nucleation of the perovskite, determination of the thin-film morphology and device performance, and protection of the perovskite and its intermediate phase against moisture during solidification. We fabricated hysteresis-free PSCs with a PCE of 21.1% and 18.0% for small and large-area blade-coated devices, comparable to that of the glovebox-processed blade-coated device. These PSCs also exhibit comparable stability to those fabricated in a glovebox. Our group also induces a multifunctional sulfobetaine-based zwitterionic surfactant to facilitate room-temperature meniscus coating of high-quality perovskite films. The systematic *in situ* study revealed the crystallization pathway of perovskite and emphasized the synergistic effects of surfactants in film formation, crystallization kinetics adjustment, defect passivation, and moisture barrier protection. The coated PSCs have negligible deterioration when the device area is upscaled to 0.8 cm^2, which is among the highest records for the upscaling coated PSCs. Besides, this method significantly improves the stability of perovskite films and devices under different aging conditions.[93–95] However, it is still challenging to deposit sub-µm thick perovskite layers from solution onto textured silicon with typical pyramids of 3–10 µm height. The Huang group demonstrated a new perovskite/silicon tandem solar cell architecture involving silicon wafers textured with pyramids less than 1 µm in height, which are rough enough

to scatter light within the silicon but smooth enough to solution process a perovskite film. The silicon bottom cell was fully textured with scalable chemistries. The sub-μm pyramids and precursor additives enabled solution-processed dense perovskite layers that fully cover the silicon texture. This tandem architecture can be adopted by silicon solar cell manufacturers, which hunt for tandem technologies with low required capital expenditures, the potential for rapid scaling, and minimum modification of their silicon cells.

For perovskite–organic tandems, large-scale fabrication also imposes requirements of large-scale OSCs. Orthogonal solvents should be used to protect the layers underneath. Otherwise, barrier layers should be designed, or a vacuum-deposition method should be utilized. Optimization of interconnection design to achieve a right balance between leakage currents and resistive losses is also indispensable for large-scale fabrication.

Stability is another essential factor for the commercialization of perovskite TSCs. For instance, the stability of perovskite–Si tandems should match the 25 year lifetime of silicon solar cells. The polycrystalline perovskite films contain a high density of defects, including point and extended imperfections, which heavily influences the devices' stability. In terms of perovskite composition (ABX_3), the X site poses photo-instability concerns; the A-site cation has a relationship with thermal, moisture, and oxygen instability. The volatile MA needs encapsulation to prevent volatilization. Besides, the narrow E_g perovskite with Sn^{2+} on the B-site has a strong tendency from the Sn^{2+} to Sn^{4+} state when exposed to oxygen or moisture. The A-site and X-site cations of perovskite are very mobile, which can also degrade stability. Photo-induced phase segregation in wide-E_g perovskite and the oxidation of Sn^{2+} to Sn^{4+} in low-bandgap are the main factors to limit the stability of PSC tandems. Admittedly, some strategies can use coordinate and ionic bonding to target the defects of the surface and grain boundaries, the conversion of those extended defects to wide E_g materials, and ion migration.[96–100] For example, our group introduced NFA molecules (IT-M) as a Lewis base to improve perovskite interfaces, which effectively enhances the electronic properties of $Cs_{0.05}(MA_{0.17}FA_{0.83})_{0.95}Pb(I_{0.83}Br_{0.17})_3$ thin films, passivates the perovskite surface defects, and further boosts the performance of PSCs. The introduction of IT-M significantly enhances the charge transport properties and boosts the photo-generated photoluminescence lifetime from 1.46 to 2.20 ms. Our group also found that the π-conjugated polymer PBDB-T triggers heterogeneous nucleation over the perovskite precursor film and passivates the trap states of the mixed perovskite through the formation of Lewis adducts between lead and oxygen atoms in PBDB-T. The p-type hydrophobic PBDB-T fills in the perovskite grain boundaries to improve charge transfer for better conductivity and prevent moisture invasion into the perovskite active layers, thus simultaneously improving efficiency and stability. However, it is still unexplored whether the phase segregation and the oxidation issues will reappear in the long term and how long the effects of the abovementioned strategies can last. Besides, the weak layer to layer adhesivity and different thermal expansion coefficients also deteriorate the perovskite

tandems' long-term stability. Currently, there are no standards of stability measurements for scientific research. The literature involving the stability of PSC tandems has different test conditions, increasing the difficulty for scientists to compare the effectiveness of different stability strategies.

Overall, through concerted efforts of materials design, device engineering, interface engineering, device physics, and improved fabrication technology and encapsulation, perovskite tandems can overcome the abovementioned challenge. Ideal perovskite-based tandem cells, especially the perovskite–silicon tandem cell, can surpass 30% efficiency and achieve good stability, to meet commercialization requirements in the near future.

Conflicts of interest

There are no conflicts to declare.

Acknowledgements

Notes and references

1 H. L. Hu, M. Singh, X. J. Wan, J. N. Tang, C. W. Chu and G. Li, Nucleation and crystal growth control for scalable solution-processed organic-inorganic hybrid perovskite solar cells, *J. Mater. Chem. A*, 2020, **8**, 1578–1603.

2 A. Kojima, K. Teshima, Y. Shirai and T. Miyasaka, Organo-metal halide perovskites as visible-light sensitizers for photovoltaic cells, *J. Am. Chem. Soc.*, 2009, **131**, 6050–6051.

3 M. Liu, M. B. Johnston and H. J. Snaith, Efficient planar heterojunction perovskite solar cells by vapour deposition, *Nature*, 2013, **501**, 395–398.

4 N. Arora, M. I. Dar, A. Hinderhofer, N. Pellet, F. Schreiber, S. M. Zakeeruddin and M. Grätzel, Perovskite solar cells with CuSCN hole extraction layers yield stabilized efficiencies greater than 20%, *Science*, 2017, **358**, 768–771.

5 Q. Jiang, Y. Zhao, X. Zhang, X. Yang, Y. Chen, Z. Chu, Q. Ye, X. Li, Z. Yin and J. You, Surface passivation of perovskite film for efficient solar cells, *Nat. Photon.*, 2019, **13**, 460–466.

6 W. Shockley and H. J. Queisser, Detailed balance limit of efficiency of p–n junction solar cells, *J. Appl. Phys.*, 1961, **32**, 510–519.

7 M. A. Green, E. D. Dunlop, J. Hohl-Ebinger, M. Yoshita, N. Kopidakis and A. W. Y. Ho-Baillie, Solar cell efficiency tables (Version 55), *Prog. Photovoltaics*, 2020, **28**, 3–15.

8 K. Yoshikawa, H. Kawasaki, W. Yoshida, T. Irie, K. Konishi, K. Nakano, T. Uto, D. Adachi, M. Kanematsu, H. Uzu and K. Yamamoto, Silicon heterojunction solar cell with interdigitated back contacts for a photoconversion efficiency over 26%, *Nat. Energy*, 2017, **2**, 17032.

9 P. Loper, S. J. Moon, S. M. de Nicolas, B. Niesen, M. Ledinsky, S. Nicolay, J. Bailat, J. H. Yum, S. De Wolf and C. Ballif, Organic–inorganic halide perovskite/crystalline silicon four-terminal tandem solar cells, *Phys. Chem. Chem. Phys.*, 2015, **17**, 1619–1629.

10 K. A. Bush, C. D. Bailie, Y. Chen, A. R. Bowring, W. Wang, W. Ma, T. Leijtens, F. Moghadam and M. D. McGehee, Thermal and environmental stability of semi-transparent perovskite solar cells for tandems enabled by a solution-processed nanoparticle buffer layer and sputtered ITO electrode, *Adv. Mater.*, 2016, **28**, 3937–3943.

11 J. Werner, G. Dubuis, A. Walter, P. Löper, S.-J. Moon, S. Nicolay, M. Morales-Masis, S. De Wolf, B. Niesen and C. Ballif, Sputtered rear electrode with broadband transparency for perovskite solar cells, *Sol. Energy Mater. Sol. Cells*, 2015, **141**, 407–413.

12 B. Chen, S.-W. Baek, Y. Hou, E. Aydin, M. De Bastiani, B. Scheffel, A. Proppe, Z. Huang, M. Wei, Y.-K. Wang, E.-H. Jung, T. G. Allen, E. Van Kerschaver, F. P. García De Arquer, M. I. Saidaminov, S. Hoogland, S. De Wolf and E. H. Sargent, Enhanced optical path and electron diffusion length enable high-efficiency perovskite tandems, *Nat. Commun.*, 2020, **11**, 1257.

13 G. E. Eperon, V. M. Burlakov, A. Goriely and H. J. Snaith, Neutral color semitransparent microstructured perovskite solar cells, *ACS Nano*, 2014, **8**, 591–598.

14 E. Della Gaspera, Y. Peng, Q. Hou, L. Spiccia, U. Bach, J. J. Jasieniak and Y.-B. Cheng, Ultra-thin high efficiency semitransparent perovskite solar cells, *Nano Energy*, 2015, **13**, 249–257.

15 Y. Yang, Q. Chen, Y.-T. Hsieh, T.-B. Song, N. D. Marco, H. Zhou and Y. Yang, Multilayer transparent top electrode for solution processed perovskite/Cu(In,Ga)(Se,S)2 four terminal tandem solar cells, *ACS Nano*, 2015, **9**, 7714–7721.

16 B. Chen, Y. Bai, Z. Yu, T. Li, X. Zheng, Q. Dong, L. Shen, M. Boccard, A. Gruverman, Z. Holman and J. Huang, Efficient semitransparent perovskite solar cells for 23.0%-efficiency perovskite/silicon four-terminal tandem cells, *Adv. Energy Mater.*, 2016, **6**, 1601128.

17 C. D. Bailie, M. G. Christoforo, J. P. Mailoa, A. R. Bowring, E. L. Unger, W. H. Nguyen, J. Burschka, N. Pellet, J. Z. Lee, M. Grätzel, R. Noufi, T. Buonassisi, A. Salleo and M. D. McGehee, Semi-transparent perovskite solar cells for tandems with silicon and CIGS, *Energy Environ. Sci.*, 2015, **8**, 956–963.

18 Z. Wang, X. Zhu, S. Zuo, M. Chen, C. Zhang, C. Wang, X. Ren, Z. Yang, Z. Liu, X. Xu, Q. Chang, S. Yang, F. Meng, Z. Liu, N. Yuan, J. Ding, S. Liu and D. Yang, 27%-Efficiency four-terminal perovskite/silicon tandem solar cells by sandwiched gold nanomesh, *Adv. Funct. Mater.*, 2020, **30**, 1908298.

19 F. Lang, M. A. Gluba, S. Albrecht, J. Rappich, L. Korte, B. Rech and N. H. Nickel, Perovskite solar cells with large-area CVD-graphene for tandem solar cells, *J. Phys. Chem. Lett.*, 2015, **6**, 2745–2750.

20 P. You, Z. Liu, Q. Tai, S. Liu and F. Yan, Efficient semitransparent perovskite solar cells with graphene electrodes, *Adv. Mater.*, 2015, **27**, 3632–3638.

21 M. Jaysankar, M. Filipič, B. Zielinski, R. Schmager, W. Song, W. Qiu, U. W. Paetzold, T. Aernouts, M. Debucquoy, R. Gehlhaar and J. Poortmans, Perovskite–silicon tandem solar modules with optimised light harvesting, *Energy Environ. Sci.*, 2018, **11**, 1489–1498.

22 H. Uzu, M. Ichikawa, M. Hino, K. Nakano, T. Meguro, J. L. Hernández, H.-S. Kim, N.-G. Park and K. Yamamoto, High efficiency solar cells combining a perovskite and a silicon heterojunction solar cells via an optical splitting system, *Appl. Phys. Lett.*, 2015, **106**, 013506.

23 J. P. Mailoa, C. D. Bailie, E. C. Johlin, E. T. Hoke, A. J. Akey, W. H. Nguyen, M. D. McGehee and T. Buonassisi, A 2-terminal perovskite/silicon multijunction solar cell enabled by a silicon tunnel junction, *Appl. Phys. Lett.*, 2015, **106**, 121105.

24 S. Albrecht, M. Saliba, J. P. Correa Baena, F. Lang, L. Kegelmann, M. Mews, L. Steier, A. Abate, J. Rappich, L. Korte, R. Schlatmann, M. K. Nazeeruddin, A. Hagfeldt, M. Grätzel and B. Rech, Monolithic perovskite/silicon-heterojunction tandem solar cells processed at low temperature, *Energy Environ. Sci.*, 2016, **9**, 81–88.

25 J. Werner, C.-H. Weng, A. Walter, L. Fesquet, J. P. Seif, S. De Wolf, B. Niesen and C. Ballif, Efficient monolithic perovskite/silicon tandem solar cell with cell area >1 cm^2, *J. Phys. Chem. Lett.*, 2016, **7**, 161–166.

26 J. Zheng, C. F. J. Lau, H. Mehrvarz, F.-J. Ma, Y. Jiang, X. Deng, A. Soeriyadi, J. Kim, M. Zhang, L. Hu, X. Cui, D. S. Lee, J. Bing, Y. Cho, C. Chen, M. A. Green, S. Huang and A. W. Y. Ho-Baillie, Large area efficient interface layer free monolithic perovskite/homo-junction-silicon tandem solar cell with over 20% efficiency, *Energy Environ. Sci.*, 2018, **11**, 2432–2443.

27 J. Zheng, H. Mehrvarz, F.-J. Ma, C. F. J. Lau, M. A. Green, S. Huang and A. W. Y. Ho-Baillie, 21.8% Efficient monolithic perovskite/homo-junction-silicon tandem solar cell on 16 cm^2, *ACS Energy Lett.*, 2018, **3**, 2299–2300.

28 J. Zheng, H. Mehrvarz, C. Liao, J. Bing, X. Cui, Y. Li, V. R. Gonçales, C. F. J. Lau, D. S. Lee, Y. Li, M. Zhang, J. Kim, Y. Cho, L. G. Caro, S. Tang, C. Chen, S. Huang and A. W. Y. Ho-Baillie, Large-area 23%-efficient monolithic perovskite/homojunction-silicon tandem solar cell with enhanced UV stability using down-shifting material, *ACS Energy Lett.*, 2019, **4**, 2623–2631.

29 H. Shen, S. T. Omelchenko, D. A. Jacobs, S. Yalamanchili, Y. Wan, D. Yan, P. Phang, T. Duong, Y. Wu, Y. Yin, C. Samundsett, J. Peng, N. Wu, T. P. White, G. G. Andersson, N. S. Lewis and K. R. Catchpole, *In situ* recombination junction between p-Si and TiO$_2$ enables high-efficiency monolithic perovskite/Si tandem cells, *Sci. Adv.*, 2018, **4**, eaau9711.

30 M. Jošt, E. Köhnen, A. B. Morales-Vilches, B. Lipovšek, K. Jäger, B. Macco, A. Al-Ashouri, J. Krč, L. Korte, B. Rech, R. Schlatmann, M. Topič, B. Stannowski and S. Albrecht, Textured interfaces in monolithic perovskite/silicon tandem solar cells: Advanced light management for improved efficiency and energy yield, *Energy Environ. Sci.*, 2018, **11**, 3511–3523.

31 L. Mazzarella, Y.-H. Lin, S. Kirner, A. B. Morales-Vilches, L. Korte, S. Albrecht, E. Crossland, B. Stannowski, C. Case, H. J. Snaith and R. Schlatmann, Infrared light management using a nanocrystalline silicon oxide interlayer in monolithic perovskite/silicon heterojunction tandem solar cells with efficiency above 25%, *Adv. Energy Mater.*, 2019, **9**, 1803241.

32 Y. Hou, E. Aydin, M. De Bastiani, C. Xiao, F. H. Isikgor, D. J. Xue, B. Chen, H. Chen, B. Bahrami, A. H. Chowdhury, A. Johnston, S. W. Baek, Z. Huang, M. Wei, Y. Dong, J. Troughton, R. Jalmood, A. J. Mirabelli, T. G. Allen, E. Van Kerschaver, M. I. Saidaminov, D. Baran, Q. Qiao, K. Zhu, S. De Wolf and E. H. Sargent, Efficient tandem solar cells with solution-processed perovskite on textured crystalline silicon, *Science*, 2020, **367**, 1135–1140.

33 B. Chen, Z. J. Yu, S. Manzoor, S. Wang, W. Weigand, Z. Yu, G. Yang, Z. Ni, X. Dai, Z. C. Holman and J. Huang, Blade-coated perovskites on textured silicon for 26%-efficient monolithic perovskite/silicon tandem solar cells, *Joule*, 2020, **4**, 850–864.

34 A. Cuevas, A. Luque, J. Eguren and J. del Alamo, 50 Per cent more output power from an albedo-collecting flat panel using bifacial solar cells, *Sol. Energy*, 1982, **29**, 419–420.

35 T. C. R. Russell, R. Saive, A. Augusto, S. G. Bowden and H. A. Atwater, The influence of spectral Albedo on bifacial solar cells: A theoretical and experimental study, *IEEE J. Photovolt.*, 2017, **7**, 1611–1618.

36 G. Coletti, S. L. Luxembourg, L. J. Geerligs, V. Rosca, A. R. Burgers, Y. Wu, L. Okel, M. Kloos, F. J. K. Danzl, M. Najafi, D. Zhang, I. Dogan, V. Zardetto, F. Di Giacomo, J. Kroon, T. Aernouts, J. Hüpkes, C. H. Burgess, M. Creatore, R. Andriessen and S. Veenstra, Bifacial four-terminal perovskite/silicon tandem solar cells and modules, *ACS Energy Lett.*, 2020, **5**, 1676–1680.

37 A. Onno, N. Rodkey, A. Asgharzadeh, S. Manzoor, Z. S. J. Yu, F. Toor and Z. C. Holman, Predicted power output of silicon-based bifacial tandem photovoltaic systems, *Joule*, 2020, **4**, 580–596.

38 O. Dupre, A. Tuomiranta, Q. Jeangros, M. Boccard, P. J. Alet and C. Ballif, Design rules to fully benefit from bifaciality in two-terminal perovskite/silicon tandem solar cells, *IEEE J. Photovolt.*, 2020, **10**, 714–721.

39 M. De Bastiani, A. J. Mirabelli, Y. Hou, F. Gota, E. Aydin, T. G. Allen, J. Troughton, A. S. Subbiah, F. H. Isikgor, J. Liu, L. J. Xu, B. Chen, E. Van Kerschaver, D. Baran, B. Fraboni, M. F. Salvador, U. W. Paetzold, E. H. Sargent and S. De Wolf, Efficient bifacial monolithic perovskite/silicon tandem solar cells via bandgap engineering, *Nat. Energy*, 2021, **6**, 167–175.

40 T. Leijtens, K. A. Bush, R. Prasanna and M. D. McGehee, Opportunities and challenges for tandem solar cells using metal halide perovskite semiconductors, *Nat. Energy*, 2018, **3**, 828–838.

41 E. T. Hoke, D. J. Slotcavage, E. R. Dohner, A. R. Bowring, H. I. Karunadasa and M. D. McGehee, Reversible photo-induced trap formation in mixed-halide hybrid perovskites for photovoltaics, *Chem. Sci.*, 2015, **6**, 613–617.

42 Z. Qiu, Z. Xu, N. Li, N. Zhou, Y. Chen, X. Wan, J. Liu, N. Li, X. Hao, P. Bi, Q. Chen, B. Cao and H. Zhou, Monolithic perovskite/Si tandem solar cells exceeding 22% efficiency via optimizing top cell absorber, *Nano Energy*, 2018, **53**, 798–807.

43 J. Xu, C. C. Boyd, Z. J. Yu, A. F. Palmstrom, D. J. Witter, B. W. Larson, R. M. France, J. Werner, S. P. Harvey, E. J. Wolf, W. Weigand, S. Manzoor, M. F. A. M. Van Hest, J. J. Berry, J. M. Luther, Z. C. Holman and M. D. McGehee, Triple-halide wide–band gap perovskites with suppressed phase segregation for efficient tandems, *Science*, 2020, **367**, 1097–1104.

44 Z. Wang, Q. Lin, F. P. Chmiel, N. Sakai, L. M. Herz and H. J. Snaith, Efficient ambient-air-stable solar cells with 2D–3D heterostructured butylammonium-caesium-formamidinium lead halide perovskites, *Nat. Energy*, 2017, **2**, 17135.

45 D. Kim, H. J. Jung, I. J. Park, B. W. Larson, S. P. Dunfield, C. Xiao, J. Kim, J. Tong, P. Boonmongkolras, S. G. Ji, F. Zhang, S. R. Pae, M. Kim, S. B. Kang, V. Dravid, J. J. Berry, J. Y. Kim, K. Zhu, D. H. Kim and B. Shin, Efficient, stable silicon tandem cells enabled by anion-engineered wide-bandgap perovskites, *Science*, 2020, **368**, 155–160.

46 A. Al-Ashouri, E. Köhnen, B. Li, A. Magomedov, H. Hempel, P. Caprioglio, J. A. Márquez, A. B. Morales Vilches, E. Kasparavicius, J. A. Smith, N. Phung, D. Menzel, M. Grischek, L. Kegelmann, D. Skroblin, C. Gollwitzer, T. Malinauskas, M. Jošt, G. Matič, B. Rech, R. Schlatmann, M. Topič, L. Korte, A. Abate, B. Stannowski, D. Neher, M. Stolterfoht, T. Unold, V. Getautis and S. Albrecht, Monolithic perovskite/silicon tandem solar cell with >29% efficiency by enhanced hole extraction, *Science*, 2020, **370**, 1300–1309.

47 I. J. Park, J. H. Park, S. G. Ji, M.-A. Park, J. H. Jang and J. Y. Kim, A three-terminal monolithic perovskite/Si tandem solar cell characterization platform, *Joule*, 2019, **3**, 807–818.

48 M. T. Hörantner, T. Leijtens, M. E. Ziffer, G. E. Eperon, M. G. Christoforo, M. D. McGehee and H. J. Snaith, The potential of multijunction perovskite solar cells, *ACS Energy Lett.*, 2017, **2**, 2506–2513.

49 J. Werner, F. Sahli, F. Fu, J. J. Diaz Leon, A. Walter, B. A. Kamino, B. Niesen, S. Nicolay, Q. Jeangros and C. Ballif, Perovskite/perovskite/silicon monolithic triple-junction solar cells with a fully textured design, *ACS Energy Lett.*, 2018, **3**, 2052–2058.

50 F. Y. Jiang, T. F. Liu, B. W. Luo, J. H. Tong, F. Qin, S. X. Xiong, Z. F. Li and Y. H. Zhou, A two-terminal

perovskite/perovskite tandem solar cell, *J. Mater. Chem. A*, 2016, **4**, 1208–1213.

51 J. H. Heo and S. H. Im, CH3NH3PbBr3–CH3NH3PbI3 perovskite–perovskite tandem solar cells with exceeding 2.2 V open circuit voltage, *Adv. Mater.*, 2016, **28**, 5121–5125.

52 Z. Chen, J. J. Wang, Y. Ren, C. Yu and K. Shum, Schottky solar cells based on CsSnI3 thin-films, *Appl. Phys. Lett.*, 2012, **101**, 093901.

53 F. Hao, C. C. Stoumpos, R. P. H. Chang and M. G. Kanatzidis, Anomalous band gap behavior in mixed Sn and Pb perovskites enables broadening of absorption spectrum in solar cells, *J. Am. Chem. Soc.*, 2014, **136**, 8094–8099.

54 Y. Li, W. Sun, W. Yan, S. Ye, H. Rao, H. Peng, Z. Zhao, Z. Bian, Z. Liu, H. Zhou and C. Huang, 50% Sn-Based planar perovskite solar cell with power conversion efficiency up to 13.6%, *Adv. Energy Mater.*, 2016, **6**, 1601353.

55 Z. Yang, A. Rajagopal, C.-C. Chueh, S. B. Jo, B. Liu, T. Zhao and A. K. Y. Jen, Stable low-bandgap Pb–Sn binary perovskites for tandem solar cells, *Adv. Mater.*, 2016, **28**, 8990–8997.

56 G. E. Eperon, T. Leijtens, K. A. Bush, R. Prasanna, T. Green, J. T.-W. Wang, D. P. McMeekin, G. Volonakis, R. L. Milot, R. May, A. Palmstrom, D. J. Slotcavage, R. A. Belisle, J. B. Patel, E. S. Parrott, R. J. Sutton, W. Ma, F. Moghadam, B. Conings, A. Babayigit, H.-G. Boyen, S. Bent, F. Giustino, L. M. Herz, M. B. Johnston, M. D. McGehee and H. J. Snaith, Perovskite–perovskite tandem photovoltaics with optimized band gaps, *Science*, 2016, **354**, 861–865.

57 W. Liao, D. Zhao, Y. Yu, C. R. Grice, C. Wang, A. J. Cimaroli, P. Schulz, W. Meng, K. Zhu, R.-G. Xiong and Y. Yan, Lead-free inverted planar formamidinium tin triiodide perovskite solar cells achieving power conversion efficiencies up to 6.22%, *Adv. Mater.*, 2016, **28**, 9333–9340.

58 W. Liao, D. Zhao, Y. Yu, N. Shrestha, K. Ghimire, C. R. Grice, C. Wang, Y. Xiao, A. J. Cimaroli, R. J. Ellingson, N. J. Podraza, K. Zhu, R.-G. Xiong and Y. Yan, Fabrication of efficient low-bandgap perovskite solar cells by combining formamidinium tin iodide with methylammonium lead iodide, *J. Am. Chem. Soc.*, 2016, **138**, 12360–12363.

59 D. Zhao, Y. Yu, C. Wang, W. Liao, N. Shrestha, C. R. Grice, A. J. Cimaroli, L. Guan, R. J. Ellingson, K. Zhu, X. Zhao, R.-G. Xiong and Y. Yan, Low-bandgap mixed tin–lead iodide perovskite absorbers with long carrier lifetimes for all-perovskite tandem solar cells, *Nat. Energy*, 2017, **2**, 17018.

60 D. Zhao, C. Chen, C. Wang, M. M. Junda, Z. Song, C. R. Grice, Y. Yu, C. Li, B. Subedi, N. J. Podraza, X. Zhao, G. Fang, R.-G. Xiong, K. Zhu and Y. Yan, Efficient two-terminal all-perovskite tandem solar cells enabled by high-quality low-bandgap absorber layers, *Nat. Energy*, 2018, **3**, 1093–1100.

61 C. Li, Z. Song, D. Zhao, C. Xiao, B. Subedi, N. Shrestha, M. M. Junda, C. Wang, C.-S. Jiang, M. Al-Jassim, R. J. Ellingson, N. J. Podraza, K. Zhu and Y. Yan, Reducing

saturation-current density to realize high-efficiency low-bandgap mixed tin–lead halide perovskite solar cells, *Adv. Energy Mater.*, 2019, **9**, 1803135.

62 Z. Yang, Z. Yu, H. Wei, X. Xiao, Z. Ni, B. Chen, Y. Deng, S. N. Habisreutinger, X. Chen, K. Wang, J. Zhao, P. N. Rudd, J. J. Berry, M. C. Beard and J. Huang, Enhancing electron diffusion length in narrow-bandgap perovskites for efficient monolithic perovskite tandem solar cells, *Nat. Commun.*, 2019, **10**, 4498.

63 R. Lin, K. Xiao, Z. Qin, Q. Han, C. Zhang, M. Wei, M. I. Saidaminov, Y. Gao, J. Xu, M. Xiao, A. Li, J. Zhu, E. H. Sargent and H. Tan, Monolithic all-perovskite tandem solar cells with 24.8% efficiency exploiting comproportionation to suppress Sn(ɪɪ) oxidation in precursor ink, *Nat. Energy*, 2019, **4**, 864–873.

64 K. Xiao, R. Lin, Q. Han, Y. Hou, Z. Qin, H. T. Nguyen, J. Wen, M. Wei, V. Yeddu, M. I. Saidaminov, Y. Gao, X. Luo, Y. Wang, H. Gao, C. Zhang, J. Xu, J. Zhu, E. H. Sargent and H. Tan, All-perovskite tandem solar cells with 24.2% certified efficiency and area over 1 cm^2 using surface-anchoring zwitterionic antioxidant, *Nat. Energy*, 2020, **5**, 870–880.

65 J. Tong, Z. Song, D. H. Kim, X. Chen, C. Chen, A. F. Palmstrom, P. F. Ndione, M. O. Reese, S. P. Dunfield, O. G. Reid, J. Liu, F. Zhang, S. P. Harvey, Z. Li, S. T. Christensen, G. Teeter, D. Zhao, M. M. Al-Jassim, M. F. A. M. van Hest, M. C. Beard, S. E. Shaheen, J. J. Berry, Y. Yan and K. Zhu, Carrier lifetimes of >1 μs in Sn–Pb perovskites enable efficient all-perovskite tandem solar cells, *Science*, 2019, **364**, 475–479.

66 Y. J. Wang, R. Wenisch, R. Schlatmann and I. Lauermann, Inorganic materials as hole selective contacts and intermediate tunnel junction layer for monolithic perovskite–CIGSe tandem solar cells, *Adv. Energy Mater.*, 2018, **8**, 18.

67 F. Fu, T. Feurer, T. P. Weiss, S. Pisoni, E. Avancini, C. Andres, S. Buecheler and A. N. Tiwari, High-efficiency inverted semi-transparent planar perovskite solar cells in substrate configuration, *Nat. Energy*, 2016, **2**, 16190.

68 F. Fu, T. Feurer, T. Jäger, E. Avancini, B. Bissig, S. Yoon, S. Buecheler and A. N. Tiwari, Low-temperature-processed efficient semi-transparent planar perovskite solar cells for bifacial and tandem applications, *Nat. Commun.*, 2015, **6**, 8932.

69 T. Todorov, T. Gershon, O. Gunawan, Y. S. Lee, C. Sturdevant, L.-Y. Chang and S. Guha, Monolithic perovskite–CIGS tandem solar cells *via in situ* band gap engineering, *Adv. Energy Mater.*, 2015, **5**, 1500799.

70 A. Guchhait, H. A. Dewi, S. W. Leow, H. Wang, G. F. Han, F. Bin Suhaimi, S. Mhaisalkar, L. H. Wong and N. Mathews, Over 20% efficient CIGS-perovskite tandem solar cells, *ACS Energy Lett.*, 2017, **2**, 807–812.

71 D. H. Kim, C. P. Muzzillo, J. Tong, A. F. Palmstrom, B. W. Larson, C. Choi, S. P. Harvey, S. Glynn, J. B. Whitaker, F. Zhang, Z. Li, H. Lu, M. F. A. M. van Hest, J. J. Berry, L. M. Mansfield, Y. Huang, Y. Yan and K. Zhu, Bimolecular additives improve wide-band-gap perovskites

for efficient tandem solar cells with CIGS, *Joule*, 2019, **3**, 1734–1745.

72 M. Nakamura, K. Tada, T. Kinoshita, T. Bessho, C. Nishiyama, I. Takenaka, Y. Kimoto, Y. Higashino, H. Sugimoto and H. Segawa, Perovskite/CIGS spectral splitting double junction solar cell with 28% power conversion efficiency, *iScience*, 2020, **23**, 101817.

73 K. Nonomura, N. J. Jeon, F. Giordano, A. Abate, T. Kinoshita, N. Joong Jeon, S. Uchida, T. Kubo, S. I. Seok, M. K. Nazeeruddin, A. Hagfeldt, M. Grätzel and H. Segawa, Spectral splitting photovoltaics using perovskite and wideband dye-sensitized solar cells, *Nat. Commun.*, 2015, **6**, 8834.

74 A. Al-Ashouri, A. Magomedov, M. Roß, M. Jošt, M. Talaikis, G. Chistiakova, T. Bertram, J. A. Márquez, E. Köhnen, E. Kasparavičius, S. Levcenco, L. Gil-Escrig, C. J. Hages, R. Schlatmann, B. Rech, T. Malinauskas, T. Unold, C. A. Kaufmann, L. Korte, G. Niaura, V. Getautis and S. Albrecht, Conformal monolayer contacts with lossless interfaces for perovskite single junction and monolithic tandem solar cells, *Energy Environ. Sci.*, 2019, **12**, 3356–3369.

75 Q. Han, Y.-T. Hsieh, L. Meng, J.-L. Wu, P. Sun, E.-P. Yao, S.-Y. Chang, S.-H. Bae, T. Kato, V. Bermudez and Y. Yang, High-performance perovskite/Cu(In,Ga)Se$_2$ monolithic tandem solar cells, *Science*, 2018, **361**, 904–908.

76 T. Todorov, T. Gershon, O. Gunawan, C. Sturdevant and S. Guha, Perovskite-kesterite monolithic tandem solar cells with high open-circuit voltage, *Appl. Phys. Lett.*, 2014, **105**, 173902.

77 Y. Li, H. Hu, B. Chen, T. Salim, Y. M. Lam, N. Yuan and J. Ding, Solution-processed perovskite-kesterite reflective tandem solar cells, *Sol. Energy*, 2017, **155**, 35–38.

78 C. Yan, S. Barlow, Z. Wang, H. Yan, A. K. Y. Jen, S. R. Marder and X. Zhan, Non-fullerene acceptors for organic solar cells, *Nat. Rev. Mater.*, 2018, **3**, 18003.

79 G. Li, W. H. Chang and Y. Yang, Low-bandgap conjugated polymers enabling solution-processable tandem solar cells, *Nat. Rev. Mater.*, 2017, **2**, 17043.

80 M. Zhang, L. Zhu, G. Zhou, T. Hao, C. Qiu, Z. Zhao, Q. Hu, B. W. Larson, H. Zhu, Z. Ma, Z. Tang, W. Feng, Y. Zhang, T. P. Russell and F. Liu, Single-layered organic photovoltaics with double cascading charge transport pathways: 18% efficiencies, *Nat. Commun.*, 2021, **12**, 309.

81 W. Ahmad, J. Khan, G. D. Niu and J. Tang, Inorganic CsPbI3 perovskite-based solar cells: A choice for a tandem device, *Sol. RRL*, 2017, **1**, 1700048.

82 Z. Yang, A. Surrente, K. Galkowski, A. Miyata, O. Portugall, R. J. Sutton, A. A. Haghighirad, H. J. Snaith, D. K. Maude, P. Plochocka and R. J. Nicholas, Impact of the halide cage on the electronic properties of fully inorganic cesium lead halide perovskites, *ACS Energy Lett.*, 2017, **2**, 1621–1627.

83 W. Chen, J. Zhang, G. Xu, R. Xue, Y. Li, Y. Zhou, J. Hou and Y. Li, A semitransparent inorganic perovskite film for overcoming ultraviolet light instability of organic solar cells and achieving 14.03% efficiency, *Adv. Mater.*, 2018, **30**, 1800855.

84 C.-C. Chen, S.-H. Bae, W.-H. Chang, Z. Hong, G. Li, Q. Chen, H. Zhou and Y. Yang, Perovskite/polymer monolithic hybrid tandem solar cells utilizing a low-temperature, full solution process, *Mater. Horiz.*, 2015, **2**, 203–211.

85 L. Zuo, X. Shi, W. Fu and A. K. Y. Jen, Highly efficient semitransparent solar cells with selective absorption and tandem architecture, *Adv. Mater.*, 2019, **31**, 1901683.

86 Z. Li, S. Wu, J. Zhang, K. C. Lee, H. Lei, F. Lin, Z. Wang, Z. Zhu and A. K. Y. Jen, Hybrid perovskite–organic flexible tandem solar cell enabling highly efficient electrocatalysis overall water splitting, *Adv. Energy Mater.*, 2020, **10**, 2000361.

87 Q. Zeng, L. Liu, Z. Xiao, F. Liu, Y. Hua, Y. Yuan and L. Ding, A two-terminal all-inorganic perovskite/organic tandem solar cell, *Sci. Bull.*, 2019, **64**, 885–887.

88 X. Chen, Z. Jia, Z. Chen, T. Jiang, L. Bai, F. Tao, J. Chen, X. Chen, T. Liu, X. Xu, C. Yang, W. Shen, W. E. I. Sha, H. Zhu and Y. Yang, Efficient and reproducible monolithic perovskite/organic tandem solar cells with low-loss interconnecting layers, *Joule*, 2020, **4**, 1594–1606.

89 Y. S. Liu, Z. R. Hong, Q. Chen, W. H. Chang, H. P. Zhou, T. B. Song, E. Young, Y. Yang, J. B. You, G. Li and Y. Yang, Integrated perovskite/bulk-heterojunction toward efficient solar cells, *Nano Lett.*, 2015, **15**, 662–668.

90 Y. Liu and Y. Chen, Integrated perovskite/bulk-heterojunction organic solar cells, *Adv. Mater.*, 2020, **32**, 1805843.

91 W. Chen, H. Sun, Q. Hu, A. B. Djurišić, T. P. Russell, X. Guo and Z. He, High short-circuit current density *via* integrating the perovskite and ternary organic bulk heterojunction, *ACS Energy Lett.*, 2019, **4**, 2535–2536.

92 H. Li and W. Zhang, Perovskite tandem solar cells: From fundamentals to commercial deployment, *Chem. Rev.*, 2020, **120**, 9835–9950.

93 K. Liu, Q. Liang, M. C. Qin, D. Shen, H. Yin, Z. W. Ren, Y. K. Zhang, H. K. Zhang, P. W. K. Fong, Z. H. Wu, J. M. Huang, J. H. Hao, Z. J. Zheng, S. K. So, C. S. Lee, X. H. Lu and G. Li, Zwitterionic-surfactant-assisted room-temperature coating of efficient perovskite solar cells, *Joule*, 2020, **4**, 2404–2425.

94 H. L. Hu, Z. W. Ren, P. W. K. Fong, M. C. Qin, D. J. Liu, D. Y. Lei, X. H. Lu and G. Li, Room-temperature meniscus coating of > 20% perovskite solar cells: A film formation mechanism investigation, *Adv. Funct. Mater.*, 2019, **29**, 1900092.

95 P. W.-K. Fong, H. Hu, Z. Ren, K. Liu, L. Cui, T. Bi, Q. Liang, Z. Wu, J. Hao and G. Li, Printing high-efficiency perovskite solar cells in high-humidity ambient environment—an in situ guided investigation, *Adv. Sci.*, 2021, **8**, 2003359.

96 P.-L. Qin, G. Yang, Z.-W. Ren, S. H. Cheung, S. K. So, L. Chen, J. Hao, J. Hou and G. Li, Stable and efficient organo-metal halide hybrid perovskite solar cells *via* π-conjugated Lewis base polymer induced trap passivation and charge extraction, *Adv. Mater.*, 2018, **30**, 1706126.

97 B. Chen, P. N. Rudd, S. Yang, Y. B. Yuan and J. S. Huang, Imperfections and their passivation in halide perovskite solar cells, *Chem. Soc. Rev.*, 2019, **48**, 3842–3867.

98 G. Yang, P. L. Qin, G. J. Fang and G. Li, A Lewis base-assisted passivation strategy towards highly efficient and stable perovskite solar cells, *Sol. RRL*, 2018, **2**, 1800055.

99 G. Kim, H. Min, K. S. Lee, D. Y. Lee, S. M. Yoon and S. I. Seok, Impact of strain relaxation on performance of α-formamidinium lead iodide perovskite solar cells, *Science*, 2020, **370**, 108–112.

100 M. Jeong, I. W. Choi, E. M. Go, Y. Cho, M. Kim, B. Lee, S. Jeong, Y. Jo, H. W. Choi, J. Lee, J. H. Bae, S. K. Kwak, D. S. Kim and C. Yang, Stable perovskite solar cells with efficiency exceeding 24.8% and 0.3 V voltage loss, *Science*, 2020, **369**, 1615.

101 B. Chen, Y. Bai, Z. Yu, T. Li, X. Zheng, Q. Dong, L. Shen, M. Boccard, A. Gruverman, Z. Holman and J. Huang, Efficient semitransparent perovskite solar cells for 23.0%-efficiency perovskite/silicon four-terminal tandem cells, *Adv. Energy Mater.*, 2016, **6**, 1601128.

102 L. Mazzarella, Y.-H. Lin, S. Kirner, A. B. Morales-Vilches, L. Korte, S. Albrecht, E. Crossland, B. Stannowski, C. Case, H. J. Snaith and R. Schlatmann, Infrared light management using a nanocrystalline silicon oxide interlayer in monolithic perovskite/silicon heterojunction tandem solar cells with efficiency above 25%, *Adv. Energy Mater.*, 2019, **9**, 1803241.